AD-A244 374

‖‖‖‖‖‖‖‖‖‖‖‖‖‖‖

WL-TR-91-30 69

INVESTIGATION OF TURBULENT JET IMPINGEMENT IN A CONFINED CROSS-
FLOW

G.D. Catalano
Department of Mechanical Engineering
LSU
Baton Rouge, LA   70803-6413

November 1, 1991

Final Report for Period September 88 - December 90

DTIC
ELECTE
JAN 16 1992
S B D

FLIGHT DYNAMICS DIRECTORATE
WRIGHT LABORATORY
AIR FORCE SYSTEMS COMMAND
WRIGHT-PATTERSON AIR FORCE BASE, OHIO   45433-6553

92-01317

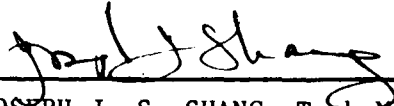‖‖‖‖‖‖‖‖‖‖‖‖‖‖‖

02 1 15 005

NOTICE

This technical report has been reviewed and is approved for publication.
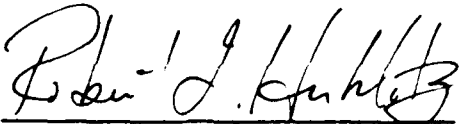

W. PHILLIP WEBSTER
Aerospace Engineer

JOSEPH J. S. SHANG, Tech Mgr
Computational Aerodynamics Group

FOR THE COMMANDER

ROBERT L. HERKLOTZ, Col, USAF
Chief
Aeromechanics Division

REPORT DOCUMENTATION PAGE

Public reporting burden for this collection of information is estimated to average 1 hour per response, including the time for reviewing instructions, searching existing data sources, gathering and maintaining the data needed, and completing and reviewing the collection of information. Send comments regarding this burden estimate or any other aspect of this collection of information, including suggestions for reducing this burden, to Washington Headquarters Services, Directorate for Information Operations and Reports, 1215 Jefferson Davis Highway, Suite 1204, Arlington, VA 22202-4302, and to the Office of Management and Budget, Paperwork Reduction Project (0704-0188), Washington, DC 20503.

1. AGENCY USE ONLY *(Leave blank)*	2. REPORT DATE November 4, 1991	3. REPORT TYPE AND DATES COVERED Final Report; 1 Sep 88 - 1 Dec 90

4. TITLE AND SUBTITLE
Investigation of Turbulent Jet Impingement in a Confined Crossflow

5. FUNDING NUMBERS
PE: 61101F
UV: ILIR #88-31
TA: 10
WV: B1
F33615-88-C-3004

6. AUTHOR(S)
George D. Catalano

7. PERFORMING ORGANIZATION NAME(S) AND ADDRESS(ES)
Louisiana State University
Mechanical Engineering Department
Baton Rouge, LA   70803-6413

8. PERFORMING ORGANIZATION REPORT NUMBER

9. SPONSORING/MONITORING AGENCY NAME(S) AND ADDRESS(ES)
W. Phillip Webster (513) 255-2551
(WL/FIMM)
Flight Dynamics Directorate
Wrig   Laboratory
Wright-Patterson AFB OH   45433-6553

10. SPONSORING/MONITORING AGENCY REPORT NUMBER
WL-TR-91-3069

11. SUPPLEMENTARY NOTES
This research was partially funded by the inhouse independent research fund.

12a. DISTRIBUTION/AVAILABILITY STATEMENT

Approved for public release; distribution is unlimited.

12b. DISTRIBUTION CODE

13. ABSTRACT *(Maximum 200 words)*

Measurements and computations are reported for the flow of a turbulent jet discharging into a crossflow confined between two parallel plates. For jet-to-crossflow velocity ratios R equal to 2 and 4, mean and fluctuating velocity components are measured by a laser-Doppler anemometer.

Higher order statistics of the streamwise velocity and its time derivative have been measured in the plane of symmetry of a jet in a confined crossflow. The existence of universal similarity of the fine scale structure of a developing turbulent velocity field and the validity of the original Kolmogorov local similarity theory and later formulations were investigated. Construction of normalized spectra for energy content, dissipation, and higher order moments enable an examination of the Reynolds number dependence of these functions for the Re_λ range from 16 to 800. Estimates of the Kolmogorov constant, μ, ranging from 0.27 to 0.43 were obtained with the arithmetic average equal to 0.38. The fractal dimension of the fine scale structure was estimated from the functional relationship between the flatness of the velocity time derivative and Re_λ. For unfiltered data, the fractal dimension was estimated to be 2.45. However, with a $\pm 12 \sigma$ bandwidth, the fractal dimension increased to 2.73.

14. SUBJECT TERMS

15. NUMBER OF PAGES
84

16. PRICE CODE

17. SECURITY CLASSIFICATION OF REPORT	18. SECURITY CLASSIFICATION OF THIS PAGE	19. SECURITY CLASSIFICATION OF ABSTRACT	20. LIMITATION OF ABSTRACT
Unclassified	Unclassified	Unclassified	

TABLE OF CONTENTS

iii

LIST OF FIGURES

LIST OF TABLES

NOMENCLATURE

C	species concentration
C_j	species concentration at the jet entrance
c_1, c_2, c_μ	constants in turbulence model
D	jet diameter at the injection
d_f	fringe spacing
d_{pv}	probe-volume diameter
$E(k)$	3-D energy spectrum function
f	frequency
$f(\tau)$	spatial correlation
$F_1(k_1)$	one dimensional spectrum function
H	channel spacing
I	integer, $I = N/M$
k	turbulent kinetic energy
K	flatness factor
k_1	wave number in x direction
l_{pv}	probe-volume length
L	longitudinal integral length scale
M	number of time delay in autocorrelation function
N	number of velocity samples
P	effective pressure, $p + 2/3\ \rho k$
p	pressure
R	velocity ratio (V_J/U_O)
R_e	Reynolds number
$R(\tau)$	autocorrelation function
S_ϕ, S_c, S_p	source terms in the governing equation
$S(f)$	auto spectral density function
S_u	skewness function
T	integral time scale
U, V, W	mean velocity components
u, v, w	fluctuating velocity components
U_O	cross stream velocity (tunnel flow speed)
V_J	jet injection velocity
x, y, z	Cartesian coordinates
y^+	dimensionless value of $y \left(= \rho k^{1/2}\ c_\mu^{1/4}\ y/\mu \right)$

Γ_Φ	diffusion coefficient
ϵ	dissipation rate of k
θ	beam-intersection angle
λ_u	under-relaxation factor
λ_{laser}	wavelength of laser beam
λ	Taylor microscale
μ	Kolmogorov Universal constant
μ_v	molecular viscosity
v	kinematic viscosity
η	Kolmogorov Length Scale
Φ	general dependent variable
Φ_1	universal energy function
Φ_ϵ	dissipation function
ρ	density
$\sigma_T, \sigma_k, \sigma_\epsilon$	turbulent Prandtl/Schmidt numbers
Ω_x	x-direction mean vorticity
τ	delay time
$(\sim)$	rms of quantity

SUMMARY

The present computational and experimental investigation demonstrates the validity of the following observations:

1) The jet trajectory and the existence of impingement are strongly dependent on the velocity ratio. For R = 2, no impingement occurs for a plate separation of ten jet diameters.

2) The cross stream is deflected laterally in the region near the jet entrance. The jet is deflected downward by the total pressure forces. The high shear around the jet edges in the near field results in a double vortex structure. The vortex structure extends far downstream.

3) A wake region exists immediately downstream of the jet discharge, but "lifts off" from the lower wall due to the strong inflow of the cross stream towards the symmetric plane.

4) The turbulence field is highly anisotropic in the initial region, although there is tendency towards isotropy further downstream.

5) The two-equation model of turbulence, with comparison to experimental data, predicts the flow downstream accurately but exhibits only fair agreement in the initial region where the flow is highly anisotropic.

The turbulent flow field obtained by injecting a jet into a confined crossflow provided a convenient case where data could be collected to examine the fine scale structure of turbulence in a developing flow over a large range of turbulent Reynolds numbers. Calculations indicated the range of turbulent Reynolds numbers to be 16.6 to 782, and the widely different values of integral length scale, varying from 0.013 to 0.438 meters confirmed the developing nature of the flow.

By directing the output of the signal processing equipment to an analog/digital converter operating in a direct memory access mode with the laboratory computer, a data collection frequency of sufficient speed to capture the fine scale fluctuations

1

was attained. The digitized velocity values were then subjected to calculation procedures designed to extract statistical estimates of certain physically relevant quantities.

Construction of normalized spectra for energy content, dissipation, and higher order moments enabled an examination of the Reynolds number dependence of these functions; the dependence was definite and well defined. Comparisons with other research data, however, indicated that this Reynolds number dependence has not been detected in some investigations of fully developed flows at comparable Reynolds numbers.

The value of the constant μ from Komogorov's lognormal hypothesis was calculated to average 0.38 over the range of turbulent Reynolds numbers sampled. Its Reynolds number dependence indicates the inappropriateness of the lognormal distribution to this flow as a whole.

The fractal dimension of the dissipative structures was estimated to be 2.45. An attempt to reconcile the discrepancy between this value and another reported estimate led to the tentative conclusion that the fractal dimension of this developing flow and the fractal dimension estimated for other developed flows encompassing a wide range of Reynolds numbers may be quite close.

INTRODUCTION

Turbulence is often referred to as the last unsolved problem in Newtonian mechanics. Turbulent motion, a flow condition in which the dependent field variables such as velocity, pressure and temperature are random both in space and time, is receiving an ever growing degree of interest among engineers and scientists. In fact, the overwhelming percentage of flows which occur in Nature or are created by Man is turbulent. Since a deterministic approach to turbulent motion is impossible due to its randomness, research in turbulent fluid mechanics has resorted to the use of experimental techniques and computational schemes.

Recent advances in diagnostic techniques have injected new momentum and excitement into turbulence research. As a consequence, a number of new aspects and insights into turbulent flows have been discovered. The existence of coherent structures is one good example. Such a discovery in turbulent flows has led to a fundamental reexamination of our understanding of turbulence. It is now commonly accepted that large-scale coherent structures play important roles in energy production, mixing and noise generation. The existence of coherent structures has been extensively reviewed by many investigators.

A number of turbulence modeling techniques together with improved numerical methods have been used as tools for the analysis of many engineering problems. Numerical methods allow systematic variations of boundary conditions and geometric variables, and also provide information on quantities of interest simultaneously and economically in cost and time. However, numerical methods cannot yet resolve details of flow physics such as scales of turbulence and other time-evolving quantities at practically occurring Reynolds numbers. Numerical methods in turbulence research supplement, rather than replace, experimental measurements.

In this study, a combined experimental and computational approach is made for the investigation of the turbulent flow field that results from the introduction of a jet

3

transversely into a confined moving stream. The flowfield is a basic configuration encountered in many real engineering problems such as V/STOL aerodynamics, the design of gas turbine combustors, the internal cooling of turbine blades, and hazardous waste disposal into bodies of water or the atmosphere. The ultimate objective of this study is to increase the understanding of the fluid dynamics involved in a jet in a confined cross flow.

The flowfield produced by a single jet discharging into a unbounded crossflow has been examined by many investigators including Crabb et al.[1], who also provided an extensive review of earlier work. One important feature of the jet in a cross stream is the deflection of the jet trajectory and the creation of a bluff body wake in the cross stream. Another feature of the flowfield is the production of a pair of counterrotating vortices created by the shear along the edges of the jet. If the velocity ratio is large enough to permit impingement on the opposite plate, additional complexities arise in the flowfield. The effect of the confining surface is examined in this work.

Turbulent jets in confined crossflows have received considerably less attention. Such configurations are relevant for many practical applications such as gas-turbine combustors, the internal cooling of turbine blades, and V/STOL aerodynamics. Stoy and Ben-Haim[2] reported measurements of jet trajectories for a single blockage ratio (H/D = 3.05) and provided empirical correlations of the impingement point in terms of the velocity ratios for $2.5 \leq R \leq 7.0$. Holdeman and Walker[3] investigated a geometry relevant to diffusion air jets in gas-turbine combustion chambers. Their measurements encompassed temperature fields for both a single jet and a row of jets in a confined crossflow. These data were then used to develop correlations characterizing the behavior of the jet in terms of flow and geometric variables. Kamotani and Greber[4] presented both velocity and temperature measurements of a single jet, a row of jets, and two opposing jets in a crossflow. The experiments were

4

performed over a wide range of velocity ratios and geometric variables. So far, no documentation of turbulent quantities for the confined problem has been provided.

This paper presents both numerical calculations and experimental results for the mean and fluctuating velocity components and scalar fields of the confined problem for jet-to-crossflow velocity ratios R of 2 an 4 at a fixed spacing between two parallel plates (H/D = 10). One aim of this study is to provide reliable measurements of the turbulent flowfield for test cases of the present calculation procedure and, as a consequence, to increase our understanding and ability to predict this complex flow.

The mean and fluctuating velocities were recorded with a laser-Doppler anemometer (LDA) system adapted for the measurement of highly turbulent flows and recirculating flows[5]. Such a system allows highly accurate, noninstrusive measurements. The calculation procedure employed a finite-difference scheme for the solution of the three-dimensional elliptic forms of the Reynolds equations. The Reynolds stresses appearing in the time-averaged equations are calculated by the two-equation model of turbulence in which the transport equations are solved for the turbulent kinetic energy k and its dissipation rate ε[6-9].

The half-circular nozzle in the bottom plate is presented in the Cartesian coordinate system by eight rectangular cells. The cell surface areas are modified so that the specified jet velocity produces the correct mass fluxes through the surface.

The applicability and the limitations of the universal similarity theory first proposed by Kolmogorov[10] with subsequent clarifications by Kolmogorov[11,12], Obukhov[13] and Yaglom[14] continue to be the focus of many investigations. A larger data base of experimental results is required in order to establish the appropriate flow conditions for such theories.

The present work seeks to examine the suitability of flow models derived from the universal similarity theories in the case of a developing flow. The models examined include the Kolmogorov (LN) model[12], the Novikov-Stewart (NS) model[15], and the

Frisch, Sulem, Nelkin (β) model[16]. The importance of the turbulent Reynolds number $\left(Re_\lambda = \frac{u\lambda}{v}\right)$ is determined for various statistical properties of the flow. Such properties include the energy and dissipation spectra, the skewness, and the kurtosis. In addition, the applicability of fractal geometry to fine scale structures in a developing flow is also examined.

For relatively high Reynolds number flows, the energy containing large scale turbulent eddies is unevenly distributed in space along with bursts of high frequency fine scale structures separated by periods of relative quiet. This observation led to refinements of Kolmogorov's first and second hypothesis by Kolmogorov[12] as well as by Obukhov[13] and Yaglom[14]. Kolmogorov's third hypothesis models as a lognormal random variable the locally averaged viscous dissipation of the turbulent kinetic energy. Mathematically:

$$\sigma^2 = A + \mu \ln (l/r) \quad \text{with } l \gg r \gg \eta \qquad (1)$$

where σ^2 is the standard deviation of the logarithm of the viscous dissipation rate, l is the integral length scale of the flow, A is a constant depending on flow geometry, r is the characteristic length of the averaging volumes, and μ is a universal constant.

The existence of a universal equilibrium range and an inertia subrange is a consequence of Kolmogorov's original theory[10-11]. The first hypothesis of similarity states that within an equilibrium range of wavenumbers there exists a nondimensional and universal function, Φ_1, such that for a locally isotopic field:

$$\Phi_1 (\eta k_1) = \frac{F_1(k_1)}{(\epsilon v^5)^{1/4}} \qquad (2)$$

where:

6

$$\overline{u_1}^2 = \int_0^\infty F_1(k_1)\,dk_1, \tag{3}$$

u_1 is the velocity fluctuation component in the mean flow direction, x_1, ϵ is the viscous dissipation of the turbulent energy, v is the kinematic viscosity, and $\eta = (v^3/\epsilon)^{1/4}$ is the Kolmogorov length scale. For this to be valid, $Re_\lambda^{3/4} >> 1$. The Reynolds number, Re_λ, used to characterize the turbulence is defined by:

$$Re_\lambda = (\overline{u_1^2})^{1/2} \lambda/v \tag{4}$$

where λ is the Taylor microscale. Kolmogorov's second hypothesis is that for an even larger Reynolds number, $Re_\lambda^{3/8} >> 1$, there exists a subrange of wavenumbers within the equilibrium region where the effects of viscosity are negligible[1-2]. The one dimensional spectrum function takes the form:

$$F_1(k_1) = \alpha_1 \epsilon^{2/3} k_1^{-5/3}. \tag{5}$$

With the assumption of a lognormal viscous dissipation according to Kolmogorov's third hypothesis[12]:

$$F_1(k_1) = \alpha_1 \epsilon^{2/3} k_1^{-5/3 - 1/9\mu} \tag{6}$$

Gurvich and Yaglom[17] provided a mathematical basis for the LN model assumptions. Gurvich and Yaglom[17] also concluded that the probability density function of any nonnegative quantity associated with the fine scale structure of turbulence is approximately lognormal with a variance similar to (1). Novikov and Stewart[15]

proposed the N-S model for the spectrum of the dissipation spectrum, Φ_ϵ, such that: $\Phi_\epsilon \propto k^{-1 + \mu}$. This was also obtained by Gurvich and Yaglom[17] for $\mu < 1$.

Frisch, Sulem and Nelkin[16] introduced the β-model of fine structure intermittency. For the β model:

$$F_1(k_1) \sim k_1^{-5/3 \, - \, 1/3\mu} \qquad (7)$$

Experimental tests of the Kolmogorov third hypothesis and attempts to evaluate the constant μ have been performed in both the laboratory and in high Reynolds number atmospheric boundary layer flows by Pond and Stewart[18], Gibson, Stegen and Williams[19], Stewart et al.[20] and Gibson, Stegen, and McConnell[21]. Averaged dissipation rates have been studied by Van Atta and Chen[22] who measured stream-line velocity derivatives for flow above the ocean. Yaglom[14] has provided a physical basis for Kolmogorov's third hypothesis. Mandelbrot[23] has shown this hypothesis to be probably untenable. A variant of the generating model leading to the log-normal has been proposed by Van Atta and Antonia[24] who have examined the influence of fluctuations in the rate of local turbulent energy dissipation on higher order structure functions for small separation distances and on moments of turbulent velocity derivatives using the hypothesis of Kolmogorov[12] and Obukhov[13]. The derivatives of the dissipation rates of turbulent velocity and temperature fields were observed by Gibson and Masiello[25] Departures from lognormality of the averaged squared derivatives were present at lower Reynolds numbers. This proved to be contrary to the proposal of Gurvich and Yaglom[17].

Experiments have yielded a wide range of values of μ. Gibson and Masiello[25] found the most probable value is within a range 0.17-0.80. Yaglom[14] estimated a value of 0.4. Antonia et al.[26] suggested a value of $\mu = 0.2$ from their investigations

of circular and plane jets along the axes of symmetry. Difficulties in comparing experimental results appear to be attributable to the questionable universality of μ.

The kurtosis or flatness of $\partial u_1/\partial x_1$ is defined as:

$$K = \overline{\left(\frac{\partial u_1}{\partial x_1}\right)}^4 \bigg/ \left[\overline{\left(\frac{\partial u_1}{\partial x_1}\right)}^2\right]^2 \tag{8}$$

Assuming local isotropy and the applicability of Taylor's hypothesis:

$$U_1 \frac{\partial u_1}{\partial t} = \frac{\partial u_1}{\partial x_1} \tag{9}$$

or

$$K = \overline{\left(\frac{\partial u_1}{\partial t}\right)}^4 \bigg/ \left[\overline{\left(\frac{\partial u}{\partial t}\right)}^2\right]^2 \tag{10}$$

EXPERIMENTAL SETUP AND MEASUREMENT SYSTEM

The experiments are performed in a subsonic wind tunnel in the Experimental Fluid Dynamics Laboratory of the Mechanical Engineering Department at Louisiana State University. The dimensions of the test section are 60 cm wide, 45 cm high, and 180 cm long. The nearly uniform flow in the test section is attained by routing the airflow through a 12:1 contraction section and flow straightening honeycomb tubes. The free stream turbulence intensity is less than 0.8% in the range of tunnel velocities (9.5 - 50.0 m/s). Optical access for the LDA measurements is provided through a removable plexiglass wall in the test section.

The jet stream is supplied from the laboratory compressed air line and adjusted by a high-precision pressure regulator. In order to minimize the effect of the tunnel wall boundary layer, the jet exit is mounted flush in a flat plate located 12 cm above the bottom wall of the tunnel and the jet is aligned with the test section center line. A top plate is similarly mounted inside the test section of the tunnel, and its distance from the wall is adjusted such that $H/D = 10$. The plates, which are made of 60-cm-wide, 180-cm-long, and 0.6-cm-thick plexiglass, have been carefully contoured at the leading edges to ensure smooth transition of the tunnel flow.

Special care is taken to obtain a flat velocity profile and low turbulence intensity at the nozzle exit. This is accomplished by use of a settling chamber, a fine mesh screen and a smooth shaped contraction section with the contraction ratio of 16: 1 through a 6.7-cm length. Variation of the mean velocity ratio values (R) is achieved by adjustment of the compressed air line pressure regulator while keeping the tunnel flow speed at 9.5 m/s. The maximum obtainable jet velocity is approximately 50.0 m/s and the corresponding Reynolds number based on the 1.27-cm jet diameter is 3.8×10^4. The Reynolds numbers investigated are 1.5×10^4 for R = 2 and 3.0×10^4 for R = 4. The assumption of the symmetry of the entire flow field about the plane, z = 0, is validated. The jet flow and the tunnel flow are seeded independently with olive

10

oil particles by use of an aerosol generator for tunnel flow and a pneumatic tool lubricator for jet flow. A laboratory schematic of the entire experimental system is presented in Figure 1.

The LDA optical arrangement (Figure 2) has been constructed from Dantec 55X Modular Optics components. A Spectra Physics Model 106-1 He-Ne laser rated at 15 mW provides a monochromatic, coherent light source of wavelength $\lambda = 632.8$ nm and beam diameter 0.68 mm at $1/e^2$ points. The beam splits into two parallel beams of equal intensity by passing through a beam splitter module. The frequency of one beam is upshifted 40 MHz by the Bragg cell which is driven by the frequency shifter. The other beam is displaced by the displacer module. The shifted frequency causes the interference fringes in the probe volume to move with a velocity $V_f = 40$ MH $\approx$ x d_f, where d_f is the fringe spacing. This capability allows the user to determine the direction of the flow.

The emerging unshifted and shifted beams pass through the backscatter section and are fed to the beam translator, which adjusts the intersection angle by reducing the beam separation distance from 60 mm to 13 mm - 39 mm. The beams then proceed through the beam expander which expands the parallel incoming beams by a factor, 1.95, and thereby decreases the size of the probe volume by the same factor, approximately quadrupling the light intensity. The beams leave the beam expander and pass through a 600-mm focal length lens which focusses them to a joint. When a beam separation distance of 39 mm is selected at the beam translator, the beam separation distance equal to 76 mm at the front lens and an intersection angle equal to 7.25° result.
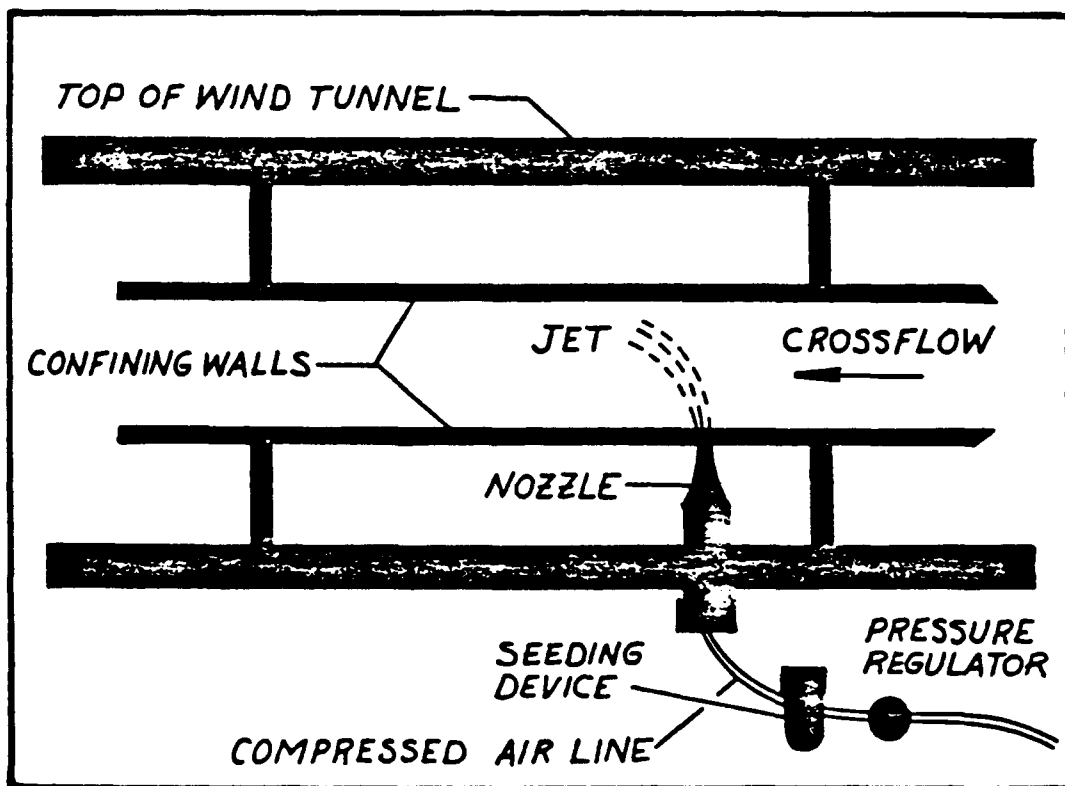
Figure 1: A Sectional View of the Flow Setup. The confining walls serve to eliminate the adverse effects of the tunnel boundary layer. A complete documentation of the mean and rms velocity fields is available in the technical literature (Catalano, et al. 1989.)
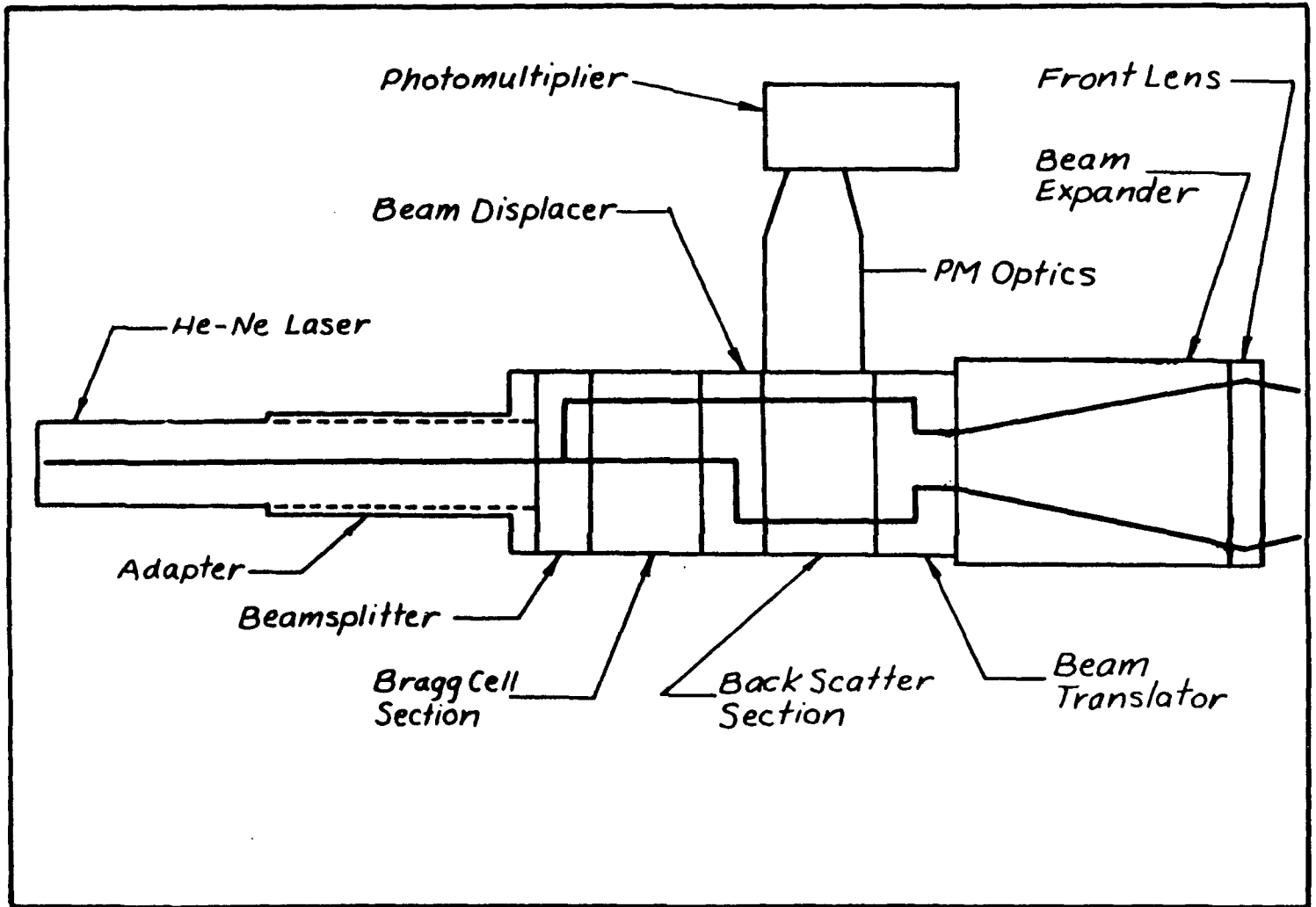
Figure 2: Schematic of the Optical Components

The light scattered from seeding particles passing through the probe volume is collected in the backward direction by the photomultiplier (PM) optics module. This module, with a 150-mm focal length lens, focuses the collected light into a pinhole aperture of 0.1-mm diameter. The PM section which acts as a spatial filter converts the photon flux to an electric signal.

The optical setup described is a one-component backward scatter system operating in the fringe-Doppler mode. The assembled LDV system can rotate 360 degrees as well as traverse in three dimensions.

The LDV actually measures the instantaneous velocity of small particles suspended in the flow. Hence, the particles must be small to follow the local velocity of the flow. As mentioned before, the wind tunnel flow and the jet stream are seeded with olive oil particles. For the seeding method used, the mean oil droplet diameter is estimated to range from 0.8 - 3.0 μm. This particle diameter range is appropriate to follow air flows where turbulence frequencies exceed 1 kHz[9].

A method for signal processing and data acquisition is vital in LDV application. The output signal from the PM consists of the sum of the Doppler frequency representing the velocity and the 40-MHz-shifted frequency. In order to achieve optimum resolution and noise filtering in the signal analysis equipment, the signal is fed to the mixer (frequency shifter) to be electronically down shifted. The effective shift of the Doppler frequency f, can be selected to a desired level from ± 10 kHz to ± 9 MHz.

The electronic mixer output signal is analyzed by a TSI Tracker Type 1090. The signals are first amplified to an optimum signal-to-noise ratio and passed through selectable band pass filters prior to the signal analysis. The high pass filters remove the DC component of the signal (pedestal) and the low pass filters remove the high frequency noise. The tracker is a phase locked loop (PLL) device. The processor locks onto the Doppler frequency and continues to track the instantaneous Doppler frequency as long as the internal servo-loop stays locked.

The continuous nature of the tracker output allows the mean and rms quantities to be read directly on appropriate meters. The signal usually contains high frequency noise. The noise is primarily due to the phase fluctuations of particles in the probe volume (called the ambiguity noise). The errors in the mean and rms velocities due to the noise are not significant. However, at a certain noise level, the tracker cannot lock onto the instantaneous Doppler frequency. The term "drop-out" refers to a condition in which the tracker is not locked onto the instantaneous frequency of the Doppler signal. The drop-out also arises in sparsely seeded flows (in high speed air flows). Fortunately, when the tracker enters the drop-out condition, a protection circuit of the tracker (sample and hold circuit) is used to lock the loop on the last measured frequency and hold the frequency until a valid Doppler signal is retrieved. Although continuous data output is recovered in this way, the errors in the mean and rms of the output are present as well as the missing of the high frequency end of the drop-out signal. These errors are referred to as statistically biased errors. Depending on the flow condition and measurement location, the velocity signal in this study exhibits either the continuous condition with high frequency noise or the drop-out condition. The drop-out signal generally arises in highly sheared regions where the rapid transition between the jet stream and the cross stream occurs.

The errors can be significantly reduced by appropriate correction methods using computer analysis. Since computers operate on discrete data points, the resulting data can be weighted by the time duration which is held between successive Doppler signals. The probability density function, autocorrelation and spectrum analysis also can be obtained by computer analysis.

The data acquisition system of this study consists of analog instruments as well as a digital system. The analog system includes an integrator, DC and rms voltmeters, and a spectrum analyzer. The digital data acquisition system is composed of a TSI Model 1090 tracker processor, a DANTEC counter used solely for amplification and

15

filtration, and a Zenith Z248 personal computer. The analog output of the tracker is sent to the computer which is equipped with an OMEGA WB-800 data acquisition A/D board. The data acquisition rate is set at 38 kHz. The number of data samples obtained and stored at each flow location is 28,400. The data records, stored on micro floppy diskettes, are transferred to the main frame, IBM 3090 computer, for statistical analysis.

As discussed in the previous section, the desirable method in the LDV measurement is to obtain the signal which is continuous in time. When the LDV is used in a large scale wind tunnel, or the speed of interest is sufficiently high, the amount of particle seeding in the flow required for continuous scattering becomes prohibitively large. In addition, the inherent noise problems in LDV applications make it difficult to obtain a continuous velocity signal. Another limiting factor, usually arising in the statistical measurements, is the storage limit of the currently available data acquisition system. This section describes the mathematical development and calculation methods of statistical parameters, with considerations of the signal drop-out and storage limit.

The moments of the instantaneous velocities are calculated by statistical analysis. The straight arithmetic averages of the moment calculations provide sufficiently accurate results when the sampled data are uniformly distributed in time. Practically, this uniform distribution is difficult to obtain. The main obstacle to this is the signal drop-out and velocity bias. Therefore, two types of correction methods are introduced, the resident time weighting for the signal drop-out and the velocity bias correction for the velocity bias. In the first method, the individual realization of the i_{th} sampled data V_i is weighted by the resident time Δt, of the realization V_i. The resident time referred to here is the time which the tracker (sample and hold circuit) holds one valid Doppler signal until a new valid signal is retrieved. The weighting is automatically achieved by selecting the sampling rate less than the drop-out period.

16

The velocity bias arises due to the proportionality of particle flux through the measurement volume to the instantaneous velocity. This fact can be easily visualized from the mass conservation of particles. This gives rise to a statistical bias towards higher velocities. Therefore, the correction factor must be the inverse of the velocity.

If V_i is the instantaneous velocity and N the number of samples taken, then the corrected forms of the moment calculations are as follows:

$$\text{Mean} = \frac{\Sigma_{i=1}^{N} V_i W_i}{\Sigma_{i=1}^{N} W_i} \tag{11}$$

$$\text{RMS} = \left[\frac{\Sigma_{i=1}^{N} \left(V_i - \overline{V}\right)^2 W_i}{\Sigma_{i=1}^{N} W_i}\right]^{1/2} \tag{12}$$

$$\text{Skewness} = \frac{\Sigma_{i=1}^{N} \left(V_i - \overline{V}\right)^3 W_i}{\sigma^3 \Sigma_{i=1}^{N} W_i} \tag{13}$$

$$\text{Flatness} = \frac{\Sigma_{i=1}^{N} \left(V_i - \overline{V}\right)^4 W_i}{\sigma^4 \Sigma_{i=1}^{N} W_i} \tag{14}$$

where W_i is the velocity bias correction function represented by $W_i = |V_i|^{-1}$, $\overline{V}$ is the mean velocity, and σ is the rms velocity (standard deviation). Discrepancies between the corrected and uncorrected averages are quantified to be a maximum 4% in the mean velocity and 7% in the rms velocity for the turbulent fluctuations up to 20%.

One further consideration in regard to the moment calculations is what sample size and sampling rate (samples per second here) provide acceptable accuracy and minimize the computational effort. The optimization of the sample size and the sampling rate is essential due to the storage limit of current data acquisition system.

17

Yanta and Smith[27] provided the approximate solution to the question of how many data are necessary to obtain good statistical parameters. Their analysis is based on the assumption that the turbulence is Gaussian (i.e. isotropic turbulence). One interesting result of their analysis is that the number of data points required is dependent upon the local flow conditions, i.e. the local turbulence intensity. For example, with 20% turbulence intensity, more than 1600 samples are required for 95% confidence limit and less than 1% error in the mean value. A similar analysis by Bates and Hughs[27] showed that the mean, rms, skewness and flatness are mainly dependent on the sample size and weakly dependent on the sampling rate. The analysis of this study on sample size and sampling rate requirements is based on these two previous studies, but is quantified by preliminary tests.

The effects of sample size on the mean, rms, skewness and flatness values are shown in Figure 3 for R = 2 at one specific point (x/D=4, y/D = 6 and z/D = 0). The sampling rate is fixed at 2 kHz for all quantities. As can be seen from the figure, no appreciable variations appear in the mean velocity and turbulence intensity curves. The variation of the mean velocity as N increases from 200 to 5200 is not noticeable and the corresponding variation of turbulence intensity is at most 0.37% (rms variation about the average turbulence intensity from N = 200 to 5200). A sample size N = 10^3 is used for the subsequent calculations of mean velocities and turbulence intensities. The errors are expected to be less than 5% for both quantities.

On the other hand, the skewness and the flatness factors only tend to converge with a sufficiently large sample size (N > 3000), and the scatter in both quantities decreases as the sample size increases. In view of this result, the sample size, N = 2560, which is used for the skewness and flatness factors, may not be sufficiently large enough to obtain highly accurate results.
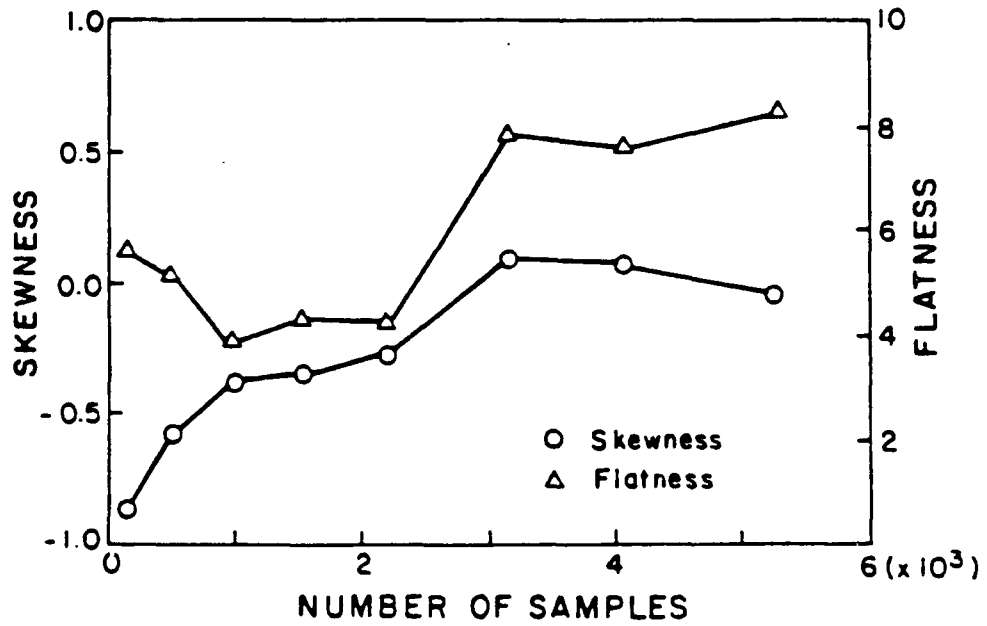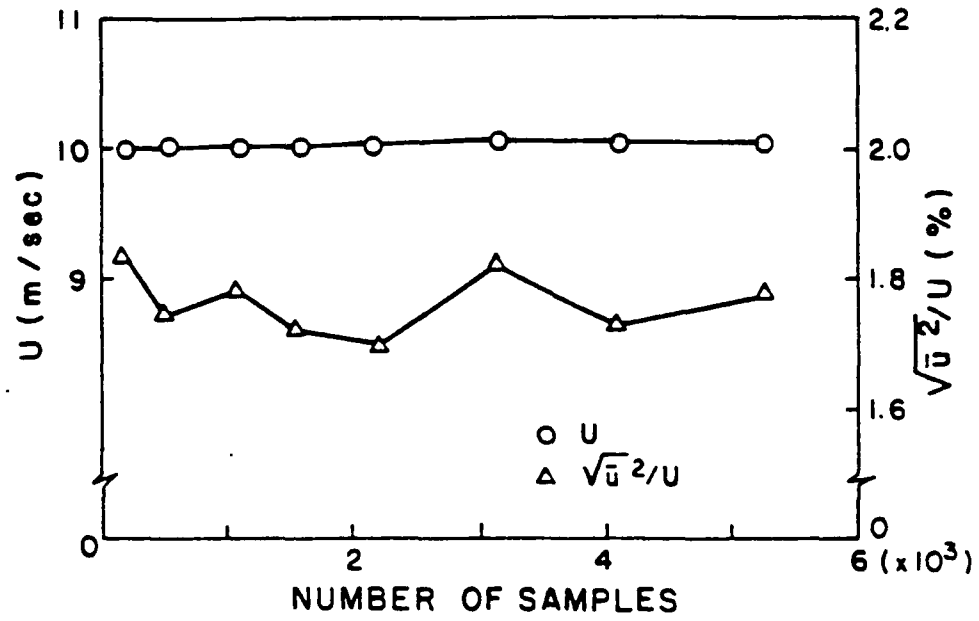
Figure 3: Effects of Sample Size on Statistical Parameters.

Since the LDV system is a one-component measurement, the Reynolds stress is calculated by averaging the projections of the velocity fluctuations in a plane. If the axis of LDA Optics rotates, for example in the x-y plane, to 0, + α, and -α degrees with respect to the x-axis at a point, the three components of the Reynolds stresses can be expressed as

$$\overline{u^2} = \overline{u_0^2} \tag{15}$$

$$\overline{u^2} = \left[\frac{\overline{u_{+\alpha}^2} + \overline{u_{-\alpha}^2}}{\sin^2(+\alpha) + \sin^2(-\alpha)} - \overline{u_0^2}\, \frac{\cos^2(+\alpha) + \cos^2(-\alpha)}{\sin^2(+\alpha) + \sin^2(-\alpha)} \right] \tag{16}$$

$$\overline{uv} = \frac{1}{2} \left[\frac{\overline{u_{+\alpha}^2} - \overline{u_{-\alpha}^2}}{\cos(+\alpha)\sin(+\alpha) + \cos(-\alpha)\sin(-\alpha)} \right] \tag{17}$$

Other components of the Reynolds stress can be obtained by projecting the instantaneous velocity components in their planes.

The calculations are executed on the IBM 3090 main frame computer after data transfer has been completed. One of the primary motivations for these statistical measurements is the acquisition of turbulent scale information. A method is devised to overcome obstacles due to limited storage space available and the existence of periods of the signal drop-out.

The autocorrelation functions are first calculated. The autocorrelation function of the longitudinal velocity component at a delay time, τ, is customarily defined as:

$$R(\tau) = \frac{\overline{u\, u}}{\overline{u^2}^{1/2}\, \overline{u^{-2}}^{1/2}} \tag{18}$$

20

where $u = u(x, y, \approx, t)$ and $u = u(x, y, \approx, t + \Delta\tau)$. The overbar in this equation denotes the time average. The autocorrelation function can be evaluated by computer analysis for each delay time, $\tau = m\Delta t$ with $m = 0, \pm 1, \pm 2, ..., \pm M$, using the data samples of $u(t)$ corresponding to $t = n\Delta t$ with $n = 0, \pm 1, \pm 2, ..., N$ or:

$$R(m\Delta t) = \frac{1}{N - 2M} \sum_{n=M}^{N-M-1} u(n\Delta t)u((n + m)\Delta t) \text{ for } |m| \leq M \tag{19}$$

where N is the total number of velocity samples and the time delay is $t = m\Delta t$. In general, the sample time, $(N - 1)\Delta t$, must be at least an order of magnitude greater than both the longest time scale of the flowfield and the maximum delay time, $\tau_{max} = (M-1)\Delta\tau$. The estimated error is proportional to $N^{-1/2}$ as N becomes large. However, for $N = IM$, and $I \geq 3$, there exists an efficient algorithm to calculate the autocorrelation function based on a Fast Fourier Transform (FFT) analysis.

The longitudinal integral scale is a convenient measure of the linear extent of the region within which velocities are appreciably correlated. Mathematically:

$$L = \int_0^{\infty} f(r)dr \tag{20}$$

where $f(r)$ is the longitudinal velocity correlation coefficient. When the longitudinal correlation coefficient cannot be directly obtained by a one-component measurement system, the integral length scale is conventionally calculated using the Taylor's hypothesis. By rewriting the Eq. 20 in terms of the autocorrelation coefficient, $R(\tau)$, we obtain:

$$L = U_c \int_0^{\infty} R(\tau)dr \tag{21}$$

21

where U_c is the local mean velocity. Typically the upper limit is chosen at the value of τ where $R(\tau)$ first crosses the τ axis.

The Taylor microscale is graphically obtained from the longitudinal correlation coefficient by fitting a parabola near the origin of the coefficient. The Taylor microscale approximately represents the eddy size where dissipation of turbulent kinetic energy is most effective by expanding $f(r)$ in a Taylor series, and by taking into account the symmetry of $f(r)$ with respect to r, the behavior of $f(r)$ in the neighborhood of the origin is expressed as:

$$f(r) = 1 + \frac{1}{2} r^2 \left[\frac{\partial^2 f}{\partial r^2}\right]_{r=0} + O\left(r^4\right) \tag{22}$$

It is common practice to define a length λ_T for very small value of r as:

$$f(r) \cong 1 - \frac{r^2}{\lambda_T^2} \tag{23}$$

The length scale λ_T is called the Taylor microscale:

$$-\frac{1}{\lambda_T^2} = \frac{1}{2} \frac{\partial^2 f(r)}{\partial r^2}\bigg|_{r \to 0} \tag{24}$$

or in terms of $R(\tau)$:

$$-\frac{1}{\lambda_T^2} = \frac{U_c}{2} \frac{\partial^2 R(\tau)}{\partial \tau^2}\bigg|_{r \to 0} \tag{25}$$

Experimentally, the Taylor microscale is obtained from this equation by numerically fitting the parabola near the origin of the curve.

22

The power spectral density function of time historic records representing a stationary random process can be defined by the Fourier transform of the correlation function. The Fourier transform of the autocorrelation function can be written as:

$$S(f) = \frac{1}{2\pi} \int_{-\infty}^{+\infty} R(\tau) e^{-j2\pi f \tau} \, d\tau$$

(26)

Then, $S(f)$ is called the auto-spectral density function. The auto-spectral density function is accomplished via a Digital Fourier Transform (DFT) originally developed by Cooley and Tukey[28]. The computer algorithm computing the DFT is available from the IMSL (International Mathematics and Scientific Language) subroutine code. This algorithm is especially applicable in cases of poor signal-to-noise ratio and periods of signal drop-out, such as is common in sparsely seeded airflows. The number of calculations required is significantly reduced when the input number of autocorrelation time steps M is represented by $M = 2^P$ where P is any integer from M^2 to M log M. The delay time step $\Delta\tau$ and the maximum time delay τ_{max} are related to the maximum frequency f_{max} (called the Nyquist cut-off frequency) and the frequency interval Δf:

$$\Delta\tau = \frac{1}{2f_{max}} \text{ and } \tau_{max} = \frac{1}{2\Delta f} \, .$$

(27)

In the present study, the autocorrelation functions are first calculated for a number of time steps M equal to 256 with the same delay time interval $\Delta\tau$ as the velocity sample time interval Δt ($\Delta\tau = \Delta t = 0.2$ msec).

Examples of the autocorrelation functions using the two different approaches, the conventional averaging technique and the direct transform method[29], are shown

23

in Figure 4. Results are presented for I = 10 and 40 (I = N/M). Note that the correlation curves become more closely aligned as I increases.

Of principal interest in this investigation, preliminary tests of length scales dependent on the sample size and on the calculation methods of autocorrelation functions are made. A comparison of the integral and Taylor microscales is presented in Figure 5 for I from 3 to 50. Several observations are appropriate. The direct transform method yields length scale values which are consistently less than those from the averaging approach. This is true for both the integral and Taylor microscales. Second, there is considerably more scatter in the computational results for the integral scale than for the microscale. One explanation for this second observation may arise in the graphical calculation of the Taylor microscale. Although a more accurate value of the Taylor microscale can be obtained with the use of a more fine scale of the delay time, a certain amount of error is included in the Taylor microscale calculations. This may overwhelm the actual variations of the Taylor microscales between two different methods. Third, the direct transform method yields a more accurate integral length scale than the averaging method when a smaller number of samples is used (I $\leq$ 20).

The near-exit plane mean velocity profiles of the jet flowfield are presented in Fig. 6 for R = 2 and R = 4. The turbulent intensities $\tilde{v}/V_J$ are equal to 5.0% for the lower value of R and equal to 1.4% for the higher value. Although not described here, the autospectra of the jet exit field did not exhibit a potential core behavior for R = 2.
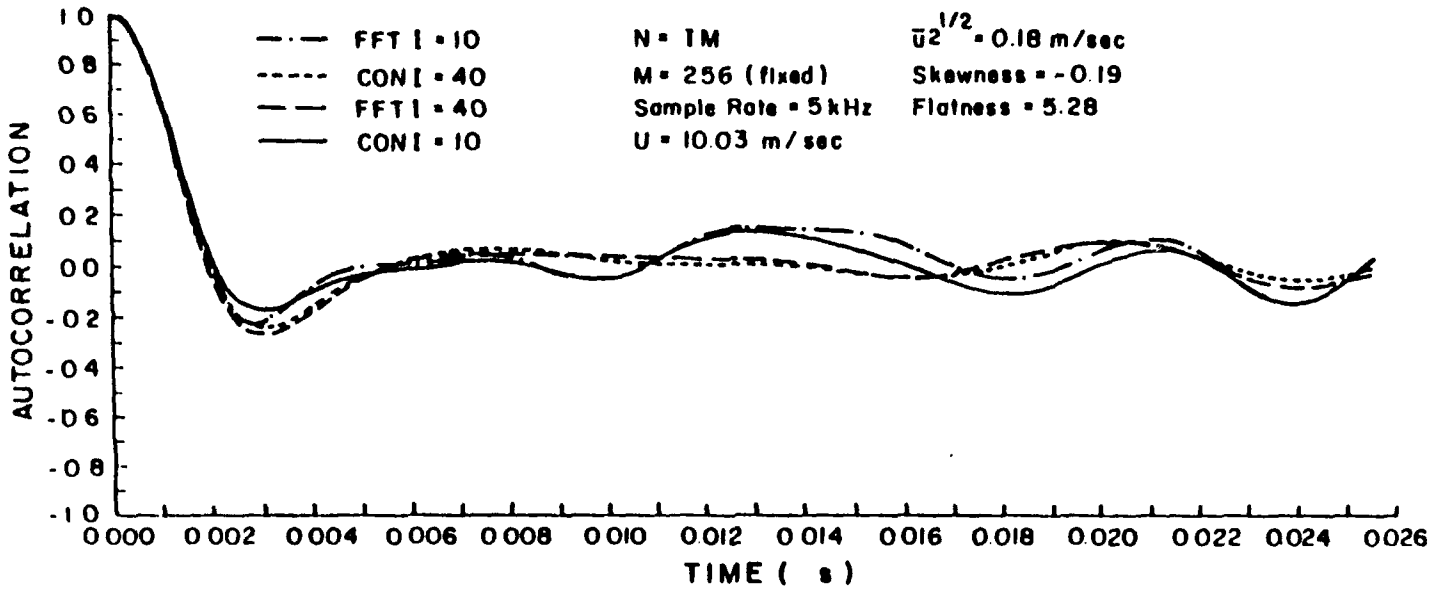
Figure 4: Comparison of Autocorrelation Functions Between Conventional Average and FFT Methods.

25
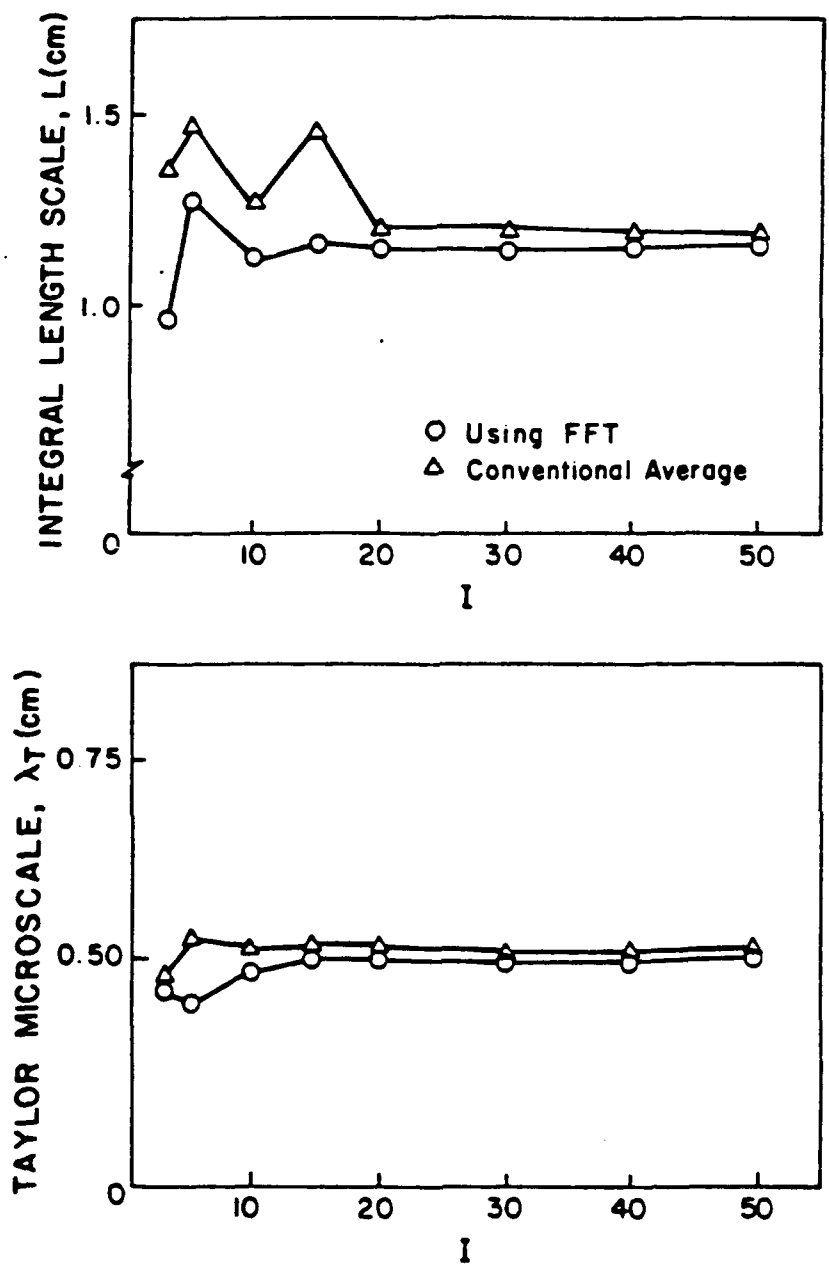
Figure 5: Comparison of Length Scales Between Conventional Average and FFT Methods for Various Sample Sizes.

26
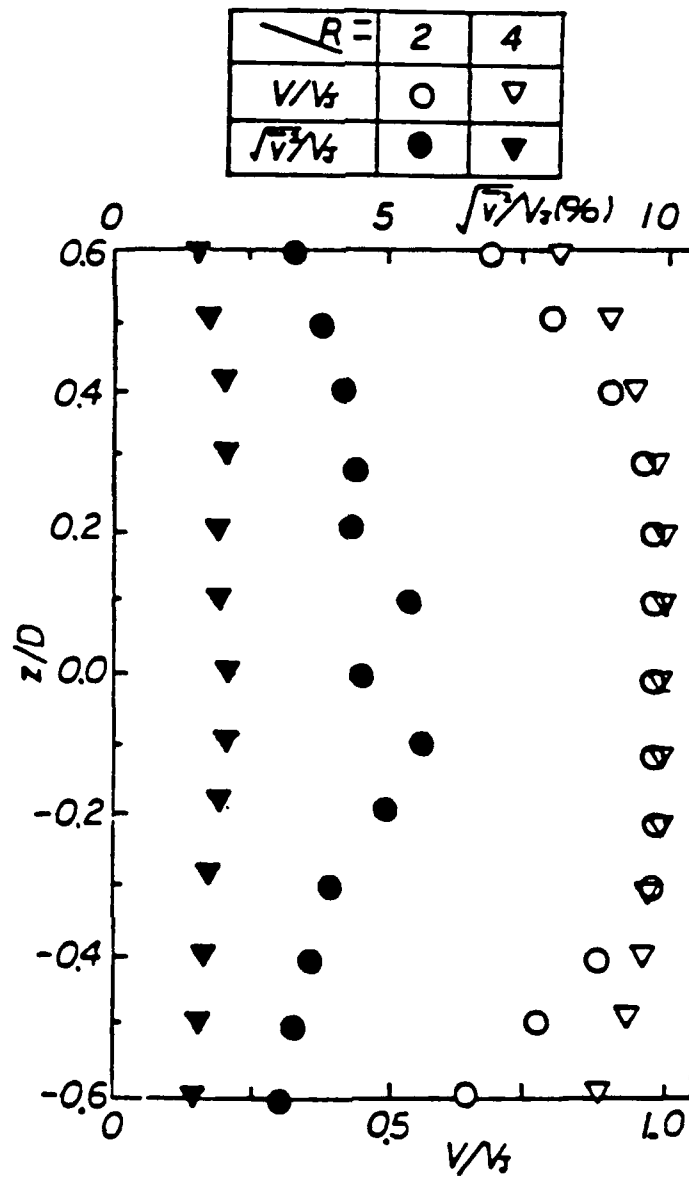
Fig. 6 Free Jet Mean Velocity Profiles at y/D = 1.0 and x/D = 0.0.

The velocity-ratio values are achieved by adjustment of the compressed-air-line pressure regulator on the jet flow system while keeping the tunnel flow fixed at 9.5 m/s. The assumption of symmetry of the entire flowfield about the plane z = 0 was also validated. In the work presented here, all of the experimental data were obtained in the plane of symmetry.

27

The details of the LDA setup are as follows:

Beam-intersection angle, θ = 7.25 deg

Fringe spacing, d_f = 5 µm

Probe-volume diameter, d_{pv} = 0.25 mm

Probe-volume length, l_{pv} = 3.6 mm

He-Ne laser rated at 15 mW, λ_{laser} = 632.8 nm.

The jet stream and the freestream are seeded with olive-oil particles using an aerosol generator. The mean oil-droplet diameter is estimated to range from 0.8 - 3.0 µm.

The difficulty in obtaining reliable measurements of small scale turbulence has been discussed by previous investigators. Tennekes and Wyngaard[31] discussed signal-to-noise and integration time limitations that make measurements of moments greater than the fourth difficult for large Reynolds number flows. Frenkiel and Klebanoff[32] discussed effects such as averaging intervals and convergent tails of the probability density functions. Champagne[33] discussed the credibility of the results of previous investigators and devised three important criteria for the elimination of results. If the length of the sensors is much greater than the Kolmogorov microscale, or the low pass filter setting is equal to or less than the Kolmogorov frequency, then the data are suspect. Additionally, inadequate averaging time results in excessive scatter. Antonia, Satyaprakash, and Hussain[34] considered two further points which were the closure of the tails of the probability density functions and the effect of Taylor's hypothesis.

Spatial resolution

The spatial resolution of the sensor is clearly important to the study of the fine structure. The ratio of length lpv(=3.6mm) to diameter dpv (=0.25mm) is 14.4. The Kolmogorov scales measured ranged from η_{min}(=0.17 mm) to η_{max} (=1.01mm). The

28

ideal sensor would require $lpv/\eta \leq 1$, and $dpv/\eta \leq 1$. In the present investigation $lpv/\eta = 21$ and $dpv/\eta = 1.5$. The correctional approach of Schedvin, Stegen, and Gibson[35] was not used. This is in agreement with the work by Antonia et al.[34].

Cut-off frequency

The cut-off frequency setting for the DANTEC filters was determined at each measurement location. It was initially set arbitrarily equal to a frequency typically twice the upper limit of the spectral content of u_1. The spectral density, Φ, obtained using a real-time spectrum analyzer was first displayed on the built-in oscilloscope of the analyzer to determine fc visually as described by Antonia et al.[34]. For the present experimental conditions, it was found that for all flow field locations, the value of fc was slightly greater than $1.5 \, f_k$.

Integration time

To reach a stable value for higher orders of moment requires a longer integration time[33]. Tennekes and Lumley[36] estimated this time by the relation:

$$w^2 = 2 \left(\frac{\overline{\dot{u}_1^{2n}}}{(\overline{\dot{u}_1^n})^2} - 1 \right) \frac{I_n}{T} \tag{25}$$

where w^2 is the mean square relative error of $\overline{\dot{u}_1^r}$, T is the total record derivation and I_n is the integral time scale of $z_n \left(\equiv \dot{u}_1^n - \overline{\dot{u}_1^n} \right)$, defined as:

$$I_n = \frac{1}{\overline{z_n^2}} \int_o^- \overline{z_n(t) \, z_n(t + \tau)} \, d\tau \tag{29}$$

Srccnivasan, Chambers, and Antonia[37] have approximated the reduction in In as n increases as

$$\frac{In}{I_1} = 0.82 - 0.07n \qquad (30)$$

In the present investigation, T (= 0.738 sec) was fixed, selecting an upperbound on the Kolmogorov microscale η (= 1 x 10^{-5}m) and $\frac{TU_1}{L_o}$ (= 1 x 10^3) (where L_o is a characteristic transverse distance) and assuming a longitudinal mean velocity U_1 (= 10m/scc), then the mean square relative error for the flatness of the velocity derivative was less than 2%. The mean square error of the skewness was similarly estimated to be less than 1%.

Convergence of p.d.f.

The average value of $\dot{u}_1^n$ can be written as:

$$\overline{\dot{u}_1^n} = \dot{u}_1^n \, p(\dot{u}_1) \, d\dot{u} \qquad (31)$$

where the probability density function:

$$\int p(\dot{u}_1) \, d\dot{u}_1 = 1 \qquad (32)$$

Careful attention must be paid to the close of the probability density function tails. Values of $\overline{\dot{u}^n}$ were computed directly from the digital record and also using the probability density function. The visual curve fits yielded results within 20% of the value obtained from the digital record. Closure of the tails of $p(\dot{u}_1)$ was reasonable even at

30

$n = 6$, thus indicating that the dynamic range of the signal processing equipment was satisfactory.

Effect of Taylor's hypotheses

Champagne[33] applied corrections to several statistics of $\dot{u}$ due to the effect of a fluctuating convection velocity on Taylor's hypotheses. An over estimate of the mean dissipation for flow locations with high turbulence results because:

$$\overline{\dot{u}_1^2} = U^2 \overline{\left(\frac{\partial u_1}{\partial x_1}\right)^2} \left(1 + \frac{\overline{u_1^2}}{U^2} + \frac{2(\overline{u_2^2} + \overline{u_3^2})}{U^2}\right) \tag{33}$$

The use of this formula in the present experimental investigation indicates that $\overline{\left(\frac{\partial u}{\partial x_1}\right)^2}$ is underestimated by about 2%. Antonia, Phan-Thien and Chambers[26] have discussed the assumptions underlying eq. (33) and concluded that since little is known about $\partial u_1/\partial x_1$, statistics of $\partial u_1/\partial x_1$ formed by decoupling $\dot{u}_1$ by $U_1 + u_1$ may be preferred. Antonia et al.[26] found that:

$$\overline{\dot{u}_1^2} = U^2 \overline{\left(\frac{\partial u_1}{\partial x_1}\right)^2} \left(1 + 3\frac{\overline{u_1^2}}{U_1^2} + 5\frac{\overline{u_1^4}}{U_1^4}\right)^{-1} \tag{34}$$

Application of this formula to the present measurement indicates that $\overline{\left(\frac{\partial u_1}{\partial x_1}\right)^2}$ is underestimated by about 2%. Antonia, Phan-Thien, and Chambers[26] noted that further work was required before a choice could be made between eqns. (33) and (34). Prior to such an investigation, no corrections have been made in the present work to either second or higher order increments as suggested by Antonia et al.[26].

31

Other Comments on Errors

The measurements and results presented in this study are meaningless without an estimate of the errors involved. The ANSI/ASME[38] procedure for calculating and reporting measurement uncertainty is followed here.

Errors are divided into three categories: calibration errors, data acquisition errors and data reduction errors. For each source of error there are a bias and a precision component. A bias error is a constant or systematic error present for the duration of the test. Precision error is random error; the measure of precision error is the statistic sample standard deviation. Error values are estimated from manufacturer's literature, by comparison of error estimates of similar equipment, by experimentation and by the author's judgement. Estimates of the various components of error are indicated in Table 1.

The total bias and precision errors are calculated by the root-sum-square method:

$$B = \left(B_1^2 + B_2^2 + B_3^2\right)^{1/2} = 0.0526 \text{ volts} \tag{35}$$

$$P = \left(P_1^2 + P_2^2 + P_3^2\right)^{1/2} = 0.0247 \text{ volts} \tag{36}$$

The final uncertainty, ψ, is obtained by combining bias and precision errors. The 95% confidence level interval[38] is given by:

$$\psi_{95} = \left(B^2 + (tP)^2\right)^{1/2} \tag{37}$$

Here, t is the student-t value and is a function of the number of degrees of freedom used in calculating P. For precision indices associated with electronic equipment[38], a large number of degrees of freedom justifies choosing t as 2.0 or:

32

$$\psi_{95} = \left[(0.0526)^2 + (2(0.0247))^2\right]^{1/2} \tag{38}$$

$$= 0.0722 \text{ volts} = 0.36 \text{ m/sec} \tag{39}$$

A velocity measurement may, therefore, be expected with a 95% confidence level to lie within ±0.36 m/sec of the experimentally obtained value. For the range of velocity values obtained in this study, this corresponds to between 13.6 and 3.40 percent error, maximum.

Table 1. Sources of Error.

<u>CALIBRATION ERROR</u>

Calibration	Bias Limit (± volts)	Precision Index (± volts)
Excitation voltage	$B_{11} = 0.0010$	$P_{11} = 0.0010$
Tracker	$B_{21} = 0.0500$	$P_{21} = 0.0200$
A/D converter	$B_{31} = 0.0020$	$P_{31} = 0.0010$

$$B_1 = \left[B_{11}^2 + B_{21}^2 + B_{31}^2\right]^{1/2} = 0.0501 \text{ volts}$$

$$P_1 = \left[P_{11}^2 + P_{21}^2 + P_{31}^2\right]^{1/2} = 0.0201 \text{ volts}$$

<u>DATA ACQUISITION ERROR</u>

Error Source	Bias Limit (± volts)	Precision Index (± volts)
Frequency shifter	$B_{12} = 0.0100$	$P_{12} = 0.0050$
Excitation voltage	$B_{22} = 0.0050$	$P_{22} = 0.0050$
Tracker	$B_{32} = 0.0100$	$P_{32} = 0.0050$
A/D converter	$B_{42} = 0.0020$	$P_{42} = 0.0020$
Atmospheric conditions	$B_{52} = 0.0000$	$P_{52} = 0.0050$
Positioning error	$B_{62} = 0.0000$	$P_{62} = 0.0100$
Velocity bias error	$B_{72} = 0.0050$	$P_{72} = 0.0000$

$$B_2 = \left[B_{12}^2 + B_{22}^2 + ... + B_{72}^2\right]^{1/2} = 0.0159 \text{ volts}$$

$$P_2 = \left[P_{12}^2 + P_{22}^2 + ... + P_{72}^2\right]^{1/2} = 0.0143 \text{ volts}$$

<u>DATA REDUCTION ERROR</u>

Error Source	Bias Limit (± volts)	Precision Index (± volts)
Computer resolution	$B_{13} = 0.0020$	$P_{13} = 0.0000$

$B_3 = 0.0020$
$P_3 = 0.0000$

MATHEMATICAL MODEL

The flow configuration is such that appreciable variations in the transported quantities such as velocity, temperature, and species arise in all these coordinate directions. It is thus necessary to solve the fully three-dimensional forms of the partial differential conservation equations for mass, momentum and energy of species concentration. Most current turbulence models rely on the solution of the so-called Reynolds time-averaged equations in which the dependent variables are decomposed into time-averaged and fluctuating components.

In Cartesian tensor notation, the time-averaged equations of continuity, momentum, and species concentration describing a steady, three-dimensional flow may be written as:

$$\frac{\partial}{\partial x_i}(\rho U_i) = 0 \tag{40}$$

$$\frac{\partial}{\partial x_j}(\rho U_j U_i) = -\frac{\partial p}{\partial x_i} + \frac{\partial}{\partial x_j}(-\rho \overline{u_i u_j}) \tag{41}$$

$$\frac{\partial}{\partial x_j}(\rho U_j C) = \frac{\partial}{\partial x_j}(-\rho \overline{u_j c}) \tag{42}$$

where ρ is the density, p is the static pressure, u and c are the fluctuating components of velocity and concentration, respectively, and U and C are the corresponding time-mean values. In the flow under consideration, molecular diffusion effects are very small compared to turbulent ones, and thus all laminar diffusion coefficients are neglected.

The time-averaged equations are exact, since no assumptions have been introduced in their derivation. However, they cannot be solved in this form, because the new stress and flux terms $(-\rho \overline{u_i u_j}$ and $-\rho \overline{u_j c})$ arising from the turbulent motion become additional unknowns. Accordingly, additional assumptions regarding the

35

relationship between the turbulent stresses and fluxes and the time mean variables must be incorporated into the turbulence model. Compilations and applications of various turbulence modeling techniques may be found in the technical literature[6]-[9].

In the k-ε model, the Reynolds stresses are related to mean straight rate via the Boussinesq eddy viscosity concept:

$$- \rho \overline{u_i u_j} = \mu_t \left(\frac{\partial U_i}{\partial x_j} + \frac{\partial U_j}{\partial x_i} \right) - \frac{2}{3} \rho \delta_{ij} k$$

(43)

where μ_t is the turbulent or eddy viscosity and $k \left(= \overline{u_i u_i} / 2 \right)$ is the turbulent kinetic energy, and δ_{ij} is the Kronecker delta. The term $\frac{2}{3} \rho k$ can be thought of as the additional pressure resulting from turbulent motion. The heat or mass flux term is obtained using the Reynolds analogy between momentum transport and energy or mass transport:

$$- \rho \overline{u_j c} = \frac{\mu_t}{\sigma_t} \frac{\partial C}{\partial x_j}$$

(44)

where σ_t is the turbulent Prandtl or Schmidt number. The σ_t is the ratio of turbulent diffusion coefficient of heat or mass transport to the corresponding momentum transport.

The system is not closed until an expression of the eddy viscosity μ_t is specified. Kolmogorov[10] suggested in the 1940s that the eddy viscosity can be evaluated as:

$$\mu_t = C_\mu \rho L k^{1/2}$$

(45)

where C_μ is an empirical constant and L is a characteristic length scale. The flow situation under consideration is such that an algebraic expression prescribing the length scale, as in the mixing length model or its modified version, is not adequate to properly simulate the complexities of the flow structure. Although a transport equa-

36

tion can be derived for a length scale, the equation is difficult to model and interpret physically. The proven applicability of the two-equation model k-ε model stems from the successful choice of length scale as $L = C_\mu k^{3/2}/\varepsilon$. The transport equations for the kinetic energy k and its dissipation rate ε are derived from the Navier-Stokes equations.

The k-ε model has been shown to provide appreciably better universality than lower order model, where the higher order closure schemes (the Reynolds stress model) appear at the moment to be insufficiently well developed to prove superior even for two-dimensional flows. It is the purpose of the computational portion of this study to apply and test the k-ε model to the prediction of the present complex three-dimensional situation. The standard version of the k-ε model proposed by Launder and Spalding[6] is used for the calculation procedure.

After few mathematical manipulations, the governing equations may be written in the following general forms:

$$\frac{\partial}{\partial x_j}\left(\rho U_j \Phi\right) = \frac{\partial}{\partial x_j}\left(\Gamma_\Phi \frac{\partial \Phi}{\partial x_j}\right) + S_\Phi$$

(46)

Equations for continuity, momentum, species concentration, turbulent kinetic energy, and dissipation rate of turbulent kinetic energy are presented in Table 2 in terms of a general dependent variable Φ, a diffusion coefficient Γ_Φ and a source term S_Φ.

Table 2: The Governing Equations

Φ	Γ_Φ	S_Φ
1	0	0
$U_i, i = 1,2,3$	μ_t	$-\dfrac{\partial P}{\partial x_1} + \dfrac{\partial}{\partial x_1}\left(\mu_t \dfrac{\partial U_1}{\partial x_1}\right)$
C	μ_t/σ_t	0
k	μ_t/σ_k	$G - \rho\varepsilon$
ε	μ_t/σ_ε	$(\varepsilon/k)(c_1 G - c_2\rho\varepsilon)$

37

$$\text{where } P = p + \frac{2}{3}\rho k$$

$$G = \mu_t \left(\frac{\partial U_1}{\partial x_j} + \frac{\partial U_1}{\partial x_1} \right) \frac{\partial U_1}{\partial x_j}$$

$$\text{and } \mu_t = C_\mu \rho k^2 / \varepsilon$$

$$C_\mu = 0.09, \ \sigma_t = 0.9, \ c_1 = 1.44$$

$$c_2 = 1.92, \ \sigma_k = 1.0, \ \sigma_\varepsilon = 1.3$$

The flow geometry under study and coordinate system are shown in Figure 1. The flow is symmetric about a vertical plane passing through the center of the jet. The calculations are therefore performed for a rectangular domain, one side of which corresponds to this symmetric plane. Computational results are obtained using a revision of the SIMPLER (Semi-Implicit Methods for Pressure-Linked Equations) algorithm. The detailed description of the algorithm is available[7], and thus only the important features of the procedure are described.

The first step of the solution procedure is the derivation of the finite-difference forms of governing equations. The finite-difference equations are first formulated by integrating the time-averaged equations over a small control volume surrounding each grid point, along with suitable assumptions about the distribution of the dependent variables between grid points. The combined effects of the convection and diffusion between grid points will be handled by the power-law scheme. The method is formulated in terms of staggered grid arrangements, in which the pressure and other variables are stored in the main grid points and the velocities in staggered locations. A two-dimensional view of staggered grid layout is shown in Figure 7. A corresponding three-dimensional grid pattern can be easily visualized in a similar manner. The staggered arrangement is necessary to avoid checkerboard pressure and velocity fields.

As a result, the general form of the finite-difference equations for scalar variables derived at the main grid point P may be written as:

$$a_P \Phi_P = a_E \Phi_E + a_W \Phi_W + a_N \Phi_N + a_S \Phi_S + a_T \Phi_T + a_B \Phi_B + b \qquad (47)$$

with:

$$a_E = D_e A(|P_e|) + [[- F_e, 0]],$$

$$a_W = D_w A(|P_w|) + [[F_w, 0]],$$

$$a_N = D_n A(|P_n|) + [[- F_n, 0]],$$

$$a_S = D_s A(|P_s|) + [[F_s, 0]],$$

$$a_T = D_t A(|P_t|) + [[- F_t, 0]],$$

$$a_B = D_b A(|P_b|) + [[F_b, 0]],$$

$$b = S_c \Delta x \Delta y \Delta z,$$

$$a_P = a_E + a_W + a_N + a_S + a_T + a_B - S_P \Delta x \Delta y \Delta z \qquad (48)$$

where Φ_P represents the general dependent variables, a's are the coefficients resulting from the combined convection and diffusion effects, and b is the source term containing all terms except the convection and diffusion terms. The upper case subscripts E, W, N, S, T and B refer to the neighborhood grid points around the main grid point P, named by east, west, north, south, top and bottom neighbor, respectively. The lower case subscripts are the corresponding control volume faces. The double bracket [[a, b]] is a special notation to denote the greater of a and b. The Peclet number P_e, which is the ratio of convection to diffusion rate, is given by:

$$P_e = \frac{F_e}{D_e} \qquad (49)$$

where F_e is the flow rate $(\rho U)_e A_e$ at the control volume face ε with an area A_e, and D_e is the diffusion conductance given by:

$$D_e = \frac{\Gamma_\Phi A_e}{(\Delta x)_e}$$

(50)

where $(\Delta x)_e$ is the control volume distance associated with the control volume face e.

The term $A(|P|)$ is the general notation categorizing various convection-diffusion schemes, such as upwind, central, hybrid, power-law, and exponential scheme. In the power-law scheme, the $A(|P|)$ may be expressed as:

$$A(|P_e|) = [[0, (1-0.1 \, |P_e|)^5]]$$

(51)

Here again the double bracket $[[\, , \,]]$ is a notation which takes the larger value of the two in the bracket. The power-law scheme provides a more realistic distribution of a convection-diffusion profile between two grid points than any other schemes except the exponential scheme. The exponential scheme, however, requires more computational time than any other convection-diffusion scheme. Notice further the source terms S_C and S_P. The source term S_Φ, originally defined in the derivation of the general form of the governing equation, is further divided into two parts such as $S_\Phi = S_C + S_P \Phi_P$. The S_C is the constant part of S_Φ, while S_P is the coefficient of Φ_P. The coefficient term S_P must be always less than or equal to zero to satisfy the stability requirement of the numerical scheme.

The finite-difference equations for the momentum equations are derived in a manner analogous to those of scalar variables, but they are formulated at the staggered locations. Special attention, however, is required for the pressure terms. Note that there is no exact equation expressing the pressure term. Focusing on U
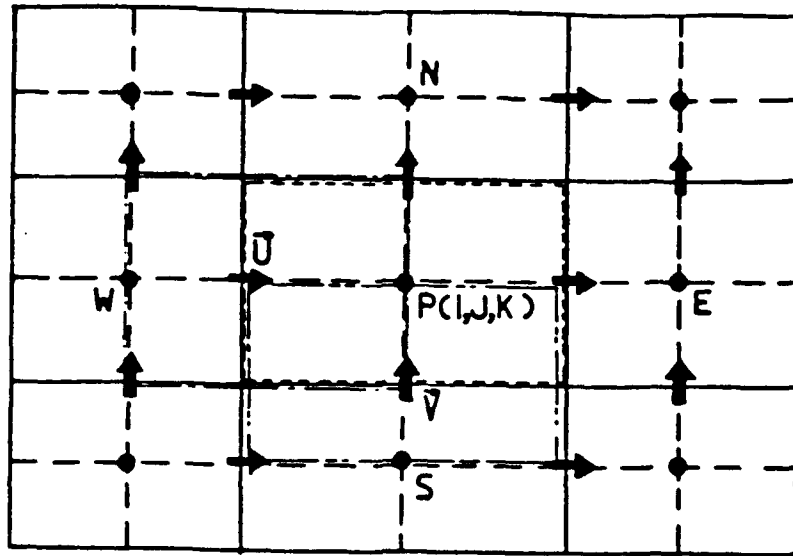
(a)
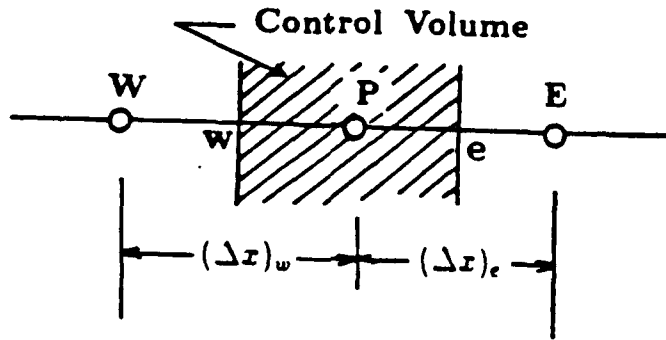
(b)

Figure 7: Grid Arrangement; (a) two-dimensional view of staggered grid layout. (b) one dimensional grid clustered for grid point P.

41

only and explicitly separating the pressure gradient from the source term, b, the resulting finite-difference equation of U derived at the control volume face e can be written as:

$$a_e U_e = \Sigma a_{nb} U_{nb} + b + (p_p - p_E) A_e \qquad (52)$$

where the summation term, $\Sigma a_{nb} U_{nb}$, denotes the sum of the neighbor terms of U_e. The momentum equation can be solved only when the pressure field is provided. Unless the correct pressure field is employed, the resulting velocity field will not satisfy the continuity equation. This problem is handled by successive iterations with an appropriate correction to the velocity field at each iteration step. A few steps of this iteration scheme will be developed.

The imperfect velocity field based on a trial pressure field (will be denoted by p') results from the solution of the following equation:

$$a_e U_e^* = \Sigma a_{nb} U_{nb}^* + b + \left(p_p^* - p_E^*\right) A_e \qquad (53)$$

The problem is now to find an appropriate correction formula to this imperfect velocity field such that the imperfect velocities in successive iterations converge, and this solution will ultimately satisfy the continuity equation. Suppose that the trial pressure field can be corrected by a pressure correction p' as:

$$p = p^* + p' \qquad (54)$$

and next the velocity field is corrected by a velocity correction $\dot{U}_e$:

$$U_e = U_e^* + \dot{U}_e \qquad (55)$$

42

Then, the relation between the pressure correction and the velocity correction can be obtained by subtracting:

$$a_e U'_e = \Sigma a_{nb} U'_{nb} + \left(p'_P - p'_E\right) A_e \tag{56}$$

The final form of the velocity correction formula is obtained by temporarily dropping the term, $\Sigma a_{nb} U'_{nb}$, from this equation and by replacing U'_e:

$$U_e = U^*_e + d_e\left(p'_P - p'_E\right) \tag{57}$$

where $d_e = A_e / a_e$. Though not presented here, the correction formula for the velocity components in other directions can be obtained in a similar manner. Now, having an expression for solving p', the system of solution scheme is essentially complete.

The p' equation is derived by substituting velocity corrections for all velocity components into the continuity equation. The p' equation is called the pressure correction equation and given by:

$$a_P p'_P = \Sigma\, a_{nb} p'_{nb} + b \tag{58}$$

where:

$$b = \left(\rho U^* A\right)_w - \left(\rho U^* A\right)_e + \left(\rho V^* A\right)_s - \left(\rho V^* A\right)_n + \left(\rho W^* A\right)_b - \left(\rho W^* A\right)_t \tag{59}$$

If b in this equation is zero, the starred velocities satisfy the continuity equation and iteration terminates. The term b thus represents a "mass source", indicating the

43

extent to which the velocity field does not satisfy mass conservation considerations at a particular iteration stage.

The solution procedures introduced up to this point are the basic algorithm of the SIMPLE methods. In an attempt to improve the rate of convergence, a revised version of SIMPLE (called SIMPLER) is more effectively worked out[7]. SIMPLER continues to use the pressure correction equation, but employs a separate pressure equation to more effectively predict the pressure field than does the SIMPLE method. The motivation for this arises from the rather exaggerated velocity corrections which are obtained by omitting the term $\Sigma a_{nb}U_{nb}$ when the p' equation is derived.

Introducing a velocity $\widehat{U}_e$ (called the "pseudo velocity") by:

$$\widehat{U}_e = \frac{\Sigma a_{nb}U_{nb} + b}{a_e} \tag{60}$$

the momentum equation for U_e can be rewritten as:

$$U_e = \widehat{U}_e + d_e(p_p - p_E) \tag{61}$$

where $d_e = A_e/a_e$. In a manner analogous to the development of the pressure correction equation, the final form of the pressure equation may be written:

$$a_p p_p = \Sigma a_{nb}p_{nb} + b \tag{62}$$

where:

$$b = \left(\rho\widehat{U}A\right)_w - \left(\rho\widehat{U}A\right)_e + \left(\rho\widehat{V}A\right)_s - \left(\rho\widehat{V}A\right)_n + \left(\rho\widehat{W}A\right)_b - \left(\rho\widehat{W}A\right)_t \tag{63}$$

44

The pressure field from this equation is a direct consequence of the given velocity field, and thus the convergence is faster than any other solution procedure containing only the pressure correction equation.

All of the equations needed for obtaining velocities, pressure and other scalar variables have been developed. The iteration procedures are now summarized. The finite-difference equations are solved by line-by-line iterations in which all the variables along a line are simultaneously solved with temporarily fixed variables lying off the line. The pressure field is first calculated, using an initially guessed or given velocity field from the previous iteration step. Then, an intermediate velocity field (starred velocities) is obtained from the momentum equation. This velocity field is once again connected to the continuity equation to obtain the pressure correction equation. This velocity field, in general, does not satisfy the continuity equation. Therefore, corrections to the velocity field are made until the latter solution satisfies both the momentum equations and the continuity equation.

The governing equations appropriate to the present flow configuration required boundary conditions for the dependent variables on all of the boundary surfaces of the solution domain. The boundaries are the inlet plane of the cross stream, the downstream plane, one symmetric plane passing through the center of the jet, one side wall, and two confining plates. Whenever the velocity is specified at a boundary, the boundary condition for the pressure is not necessary, because only the relative magnitude of pressure force plays a role in the momentum equations.

The upstream boundary conditions are prescribed, as far as possible, from the experimental measurements. These data include the x-component mean velocity, the turbulent kinetic energy, and the length scale. At the symmetric plane, Neumann boundary conditions are applied, i.e., the normal gradients of all variables except the normal velocity component are taken to be zero. The normal velocity is set to zero (W = 0).

At the downstream plane the gradients of all dependent variables in the x-direc-tion are equal to zero. These conditions may not correspond to those prevailing in the real flow. The conditions are satisfactory only when the fully developed profile assumptions of the variables are valid. This requirement locates the boundary unnecessarily far downstream (for example, x/D > 100 with R = 6). Practically, the boundary location is adjusted such that the specified boundary conditions, which in a certain range differ from the fully-developed conditions, have negligible influence in the region of interest. For the variations of all dependent variables less than 1%, the conditions are achieved by computational trials, approximately at x/D = 24 for R = 2, x/D = 32 for R = 4, and x/D = 48 for R = 6.

The boundary conditions on the walls require special considerations. This is primarily due to the significant effects of molecular viscosity. Note that the two-equation model of turbulence previously introduced has neglected the molecular viscosity. The neglect of molecular viscosity is valid only in the fully turbulent regions. A two-layer model of the wall function method proposed by Launder and Spalding[6] is utilized in the present computational study. Usual no-slip conditions are still valid for the convection fluxes. For the two velocity components parallel to the wall, the diffusion fluxes are patched onto the wall law profiles:

$$\mu_{eff} = \mu \quad \text{if} \quad y^+ < 11.5 \tag{64}$$

and:

$$\mu_{eff} = \frac{\mu y+}{(1/\kappa)\ln(Ey+)} \quad \text{if} \quad y^+ \geq 11.5 \tag{65}$$

where κ is the Von-Karman constant (= 0.41) and E is another constant with a value of 9.0. The y+ is the normalized distance of the first internal grid point from the wall, defined by:

$$y^+ = \rho k^{1/2} C_\mu^{1/4} \frac{y_1}{\mu}$$

where y_1 is the actual distance of the grid from the wall. Because of the considerable variations of turbulent quantities near the wall, the mean generation rate $\overline{G}$ and the mean dissipation rate $\overline{\epsilon}$ of the turbulent kinetic energy appearing in the governing turbulent kinetic equation (Table 2) are evaluated using the profile assumptions of the turbulent quantities near the wall cell.

All of the dependent variables also must be specified at the jet exit plane. The half-circular nozzle, however, is modified by the rectangular cells in the Cartesian coordinate system (Figure 8). The cell surface areas are adjusted such that the specified jet velocity provides the correct mass flux through the surface. In order to investigate the influence of the jet boundary conditions on the computed results, two different profiles are tested as the jet field initial conditions for R = 2 and 4. The first is the uniform profile (top hat shape in Figure 9), characterizing the flow exiting a contraction/nozzle arrangement. The second profile maintains the same momentum flux, but is skewed downstream.

The velocity and species concentration profiles used for the second condition are from the measurements by Andreopoulos[39,40]. His measurements revealed that the jet stream at the exit plane is distorted due to the pressure gradients across the plane and the distortion increases as the velocity ratio R decreases. Figure 10 shows the longitudinal mean velocity profiles nondimensionalized with the free stream value, U/U_o, plotted versus vertical distance. The maximum deviation of U/U_o between two conditions at x/D = 0.0 is at most 6% for both velocity ratios. After x/D > 2, there are essentially negligible differences between profiles with two different boundary conditions. Though not depicted here, the same observations are correct for the profiles of the scalar concentration field.
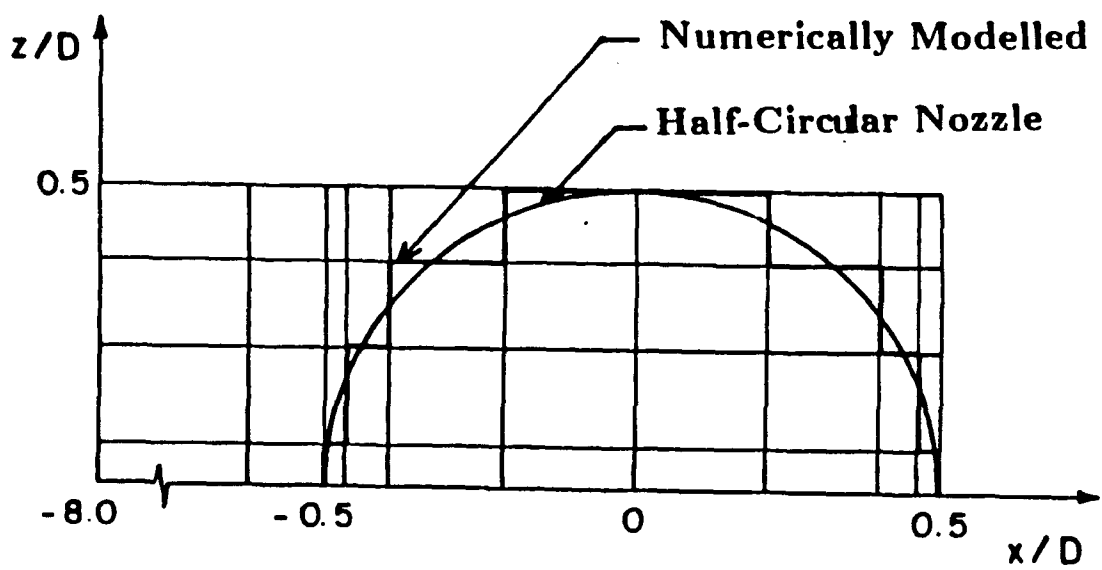
47

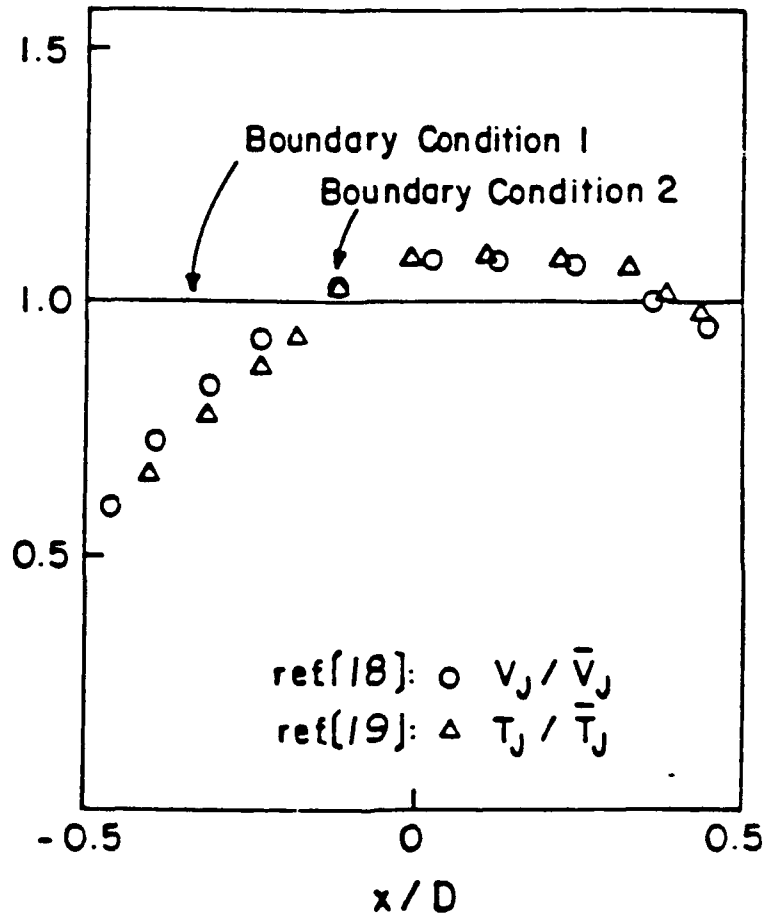Figure 8: Modification of the Half-Circular Nozzle by Rectangular Cells.

48

Figure 9: Mean Velocity and Temperaure Profiles at the Jet Exit Plane for R = 2.

One conclusion reached from these observations is that only the total momentum flux at the jet exit plane (not its profiles) is important for the development of the flow field downstream. Physically, this means that near the jet discharge the flow field is not significantly influenced by viscous effects, so that the viscous diffusion due to the velocity gradients at the jet exit plane may be neglected. The first boundary condition is chosen for the subsequent calculations because it is the simplest and most generally used in computational situations. Particularly for the flow situation under study, the realistic profile of the second condition is not expected to provide appreciably better results over the first, simpler one.

The boundary conditions described above are tabulated in Table 3. In this table, W(T/B) denotes the wall function applied both to the top and bottom walls, and W(S) applied to the side wall. At all grid points near the wall, the local equilibrium values of the turbulent quantities replace the dissipation rate ε, instead of solving it from the transport equation. The equilibrium profile is given in the bottom right corner in Table 3. The isotropic assumption is used for the boundary condition of the turbulent kinetic energy at the upstream boundary plane.

Table 3: A Summary of Boundary Conditions

	Upstream	Downstream	Symmetry	Jet exit	Walls
U	U_0	$\partial U/\partial x = 0$	$\partial U/\partial z = 0$	0	W(S), W(T/B)
V	0	$\partial V/\partial x = 0$	$\partial V/\partial z = 0$	0	W(S)
W	0	$\partial W/\partial x = 0$	0	V_J	W(T/B)
C	0	$\partial C/\partial x = 0$	$\partial C/\partial z = 0$	1	$\partial C/\partial N$ *
k	$(3/2)u_0^2$	$\partial k/\partial x = 0$	$\partial k/\partial z = 0$	$(1/2)(v_J^2)$	W(S), W(T/B)
ε	$k^{3/2}/(0.165H)$	$\partial \varepsilon/\partial x = 0$	$\partial \varepsilon/\partial z = 0$	$k^{3/2}/(0.5D)$	$(C_\mu^{3/4} k^{3/2})/(\kappa y_1)$ **

*Impermeable wall boundary condition
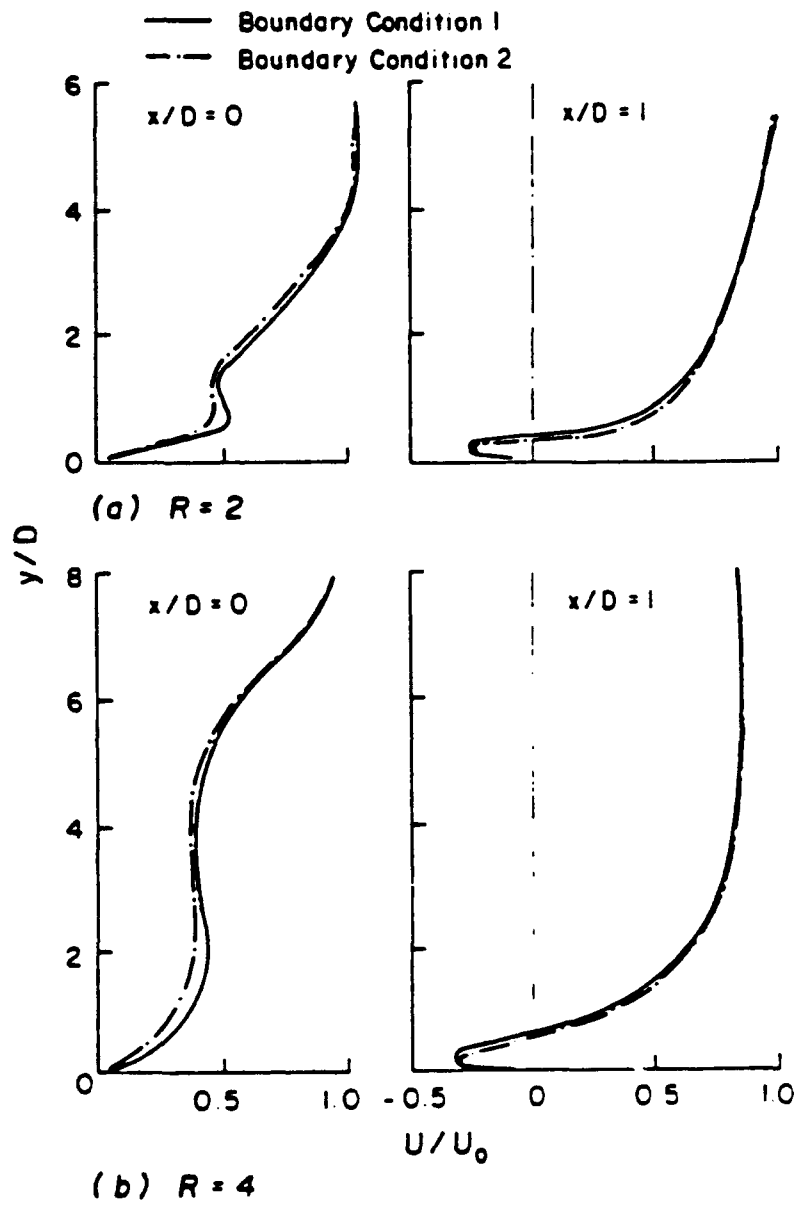**Local equilibrium profile specified on the grids nearest the wall

50

Figure 10:   Comparison of Mean Velocity U/U_0 between two different Jet Exit Boundary Conditions in the Plane of Symmetry; (a) R = 2; (b) R = 4.

51

The computations are executed on an IBM 3090 at Louisiana State University. In order to minimize the number of grid points to be used, nonuniform spacing is used so that grid nodes could be clustered where rapid variations of dependent variables are expected. This means that fine grid spacing is used near the jet discharge, and an increasingly larger grid spacing is used away from the discharge hole in all three coordinate directions. The location of the grid line nearest the wall is adjusted such that all grid points on the line occur in the fully turbulent region ($11 < y^+ < 300$) where the logarithmic wall law profiles are valid.

At each iteration it is necessary to employ under-relaxation when solving the algebraic, finite-difference equations (i.e., $\Phi = \lambda_\Phi \Phi_{new} + (1 - \lambda_\Phi)\Phi_{old}$). The number of iterations and the stability or divergence of the solutions are directly affected by the value of the under-relaxation factor λ_Φ. Typical values of λ_Φ used are $\lambda_\Phi = 0.2$ to 0.4 for the velocity components and $\lambda_\Phi = 0.5$ for all scalar variables. The iteration terminates when the normalized sum of the mass source with respect to inflow mass flux (b in Eq. 4.30), which represents the deviation of the velocity field from the mass conservation, is less than 10^{-5} and the variations of all dependent variables between two successive iterations are less than 0.1%. A typical calculation using 20 x 15 x 15 points (x, y and z direction, respectively) required approximately 250 iterations and 14 minutes of CPU time.

Computer storage limitations in the 3-D calculation necessitate the use of a relatively coarse grid distribution. The actual variations of the dependent variables between grid points in the convection-diffusion problems exhibit an exponential behavior (power-law scheme represents this behavior). A truncated Taylor series in an upwind or central difference scheme fails to be an adequate representation of the exponential behavior except for fine grid size[7]. The power-law scheme adapted in this work provides an acceptable representation of the exponential behavior and therefore minimizes false diffusion. Demuren[8] provides estimation methods of false

diffusion in 3-D calculations. However, for the present work, with the computer storage available at this time, it is difficult to refine the finite-difference grid further. There are, however, indications that the results are grid dependent, as the contour shapes are repeatable with a coarser grid size (15 x 10 x 10 in the x, y and z directions, respectively) but the magnitude of, for example, the x-component of mean velocity may vary up to 10%.

RESULTS

The jet-to-cross-stream velocity ratios (R) investigated were 2 and 4. The spacing between the parallel plates is fixed at 10 jet diameters and each side wall is located 15 jet diameters from the jet center. Figure 11 shows isocontour plots of the nondimensionalized species concentration C/C_J in the plane of symmetry. The contours indicate the extent of the penetration of the marked jet particles into the outer stream. With the presentation of the isocontours, the line S of maximum maximorum (i.e., maximum of maximums) is identified. From this line, a qualitative representation of the flowfield is achieved including the extent of the jet deflection and the existence of impingement. Note that impingement does not occur for R = 2. Total mean velocity vectors in the plane of symmetry of the flowfield are shown in Figure 12. With R = 4, significant upward motion continues farther downstream. For the case of R = 2, the jet is deflected downward near the jet discharge and more rapidly aligned with the cross stream. Note the wake regions in the outer flow immediately upstream and downstream of the jet entrance.

The predicted isocontours of the scalar field at three transverse cross sections downstream are presented in Figure 13 for both the velocity ratios of 2 an 4. The top wall is not shown for R = 2. The results indicate that the diffusion characteristics of the jet stream strongly depend on the velocity ratio. For the lower velocity ratio, the jet is deflected rapidly by the influence of the cross-stream momentum. The jet stream is convected downstream and diffuses out in both the vertical and transverse
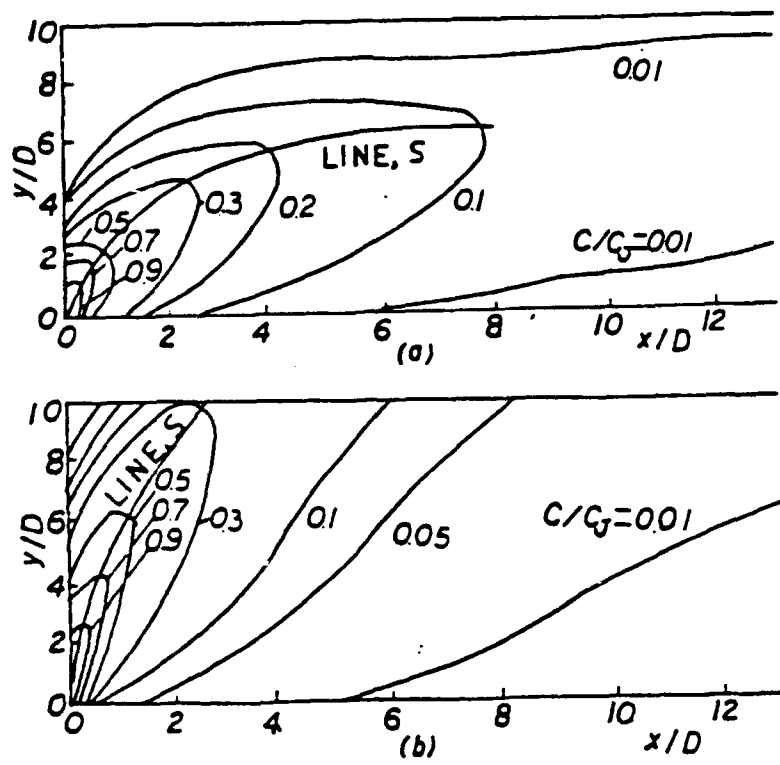
54

Figure 11: Dimensionless Scalar Field C/C_j and Line of Maximum Maximorum, S, in x-y plane (z = 0): a) R = 2; and b) R = 4.
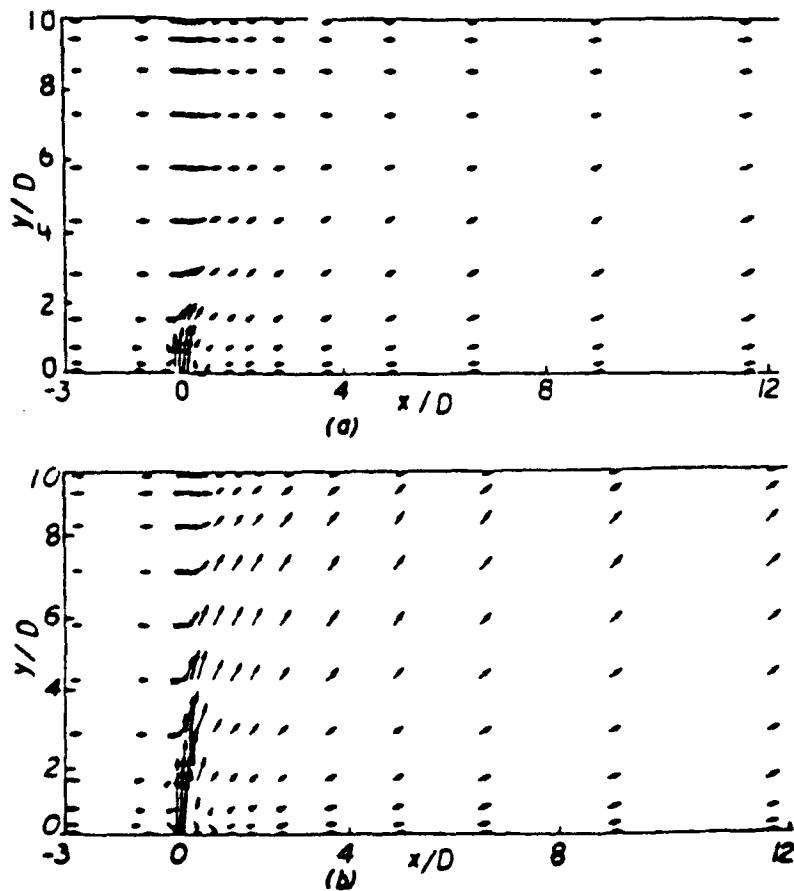

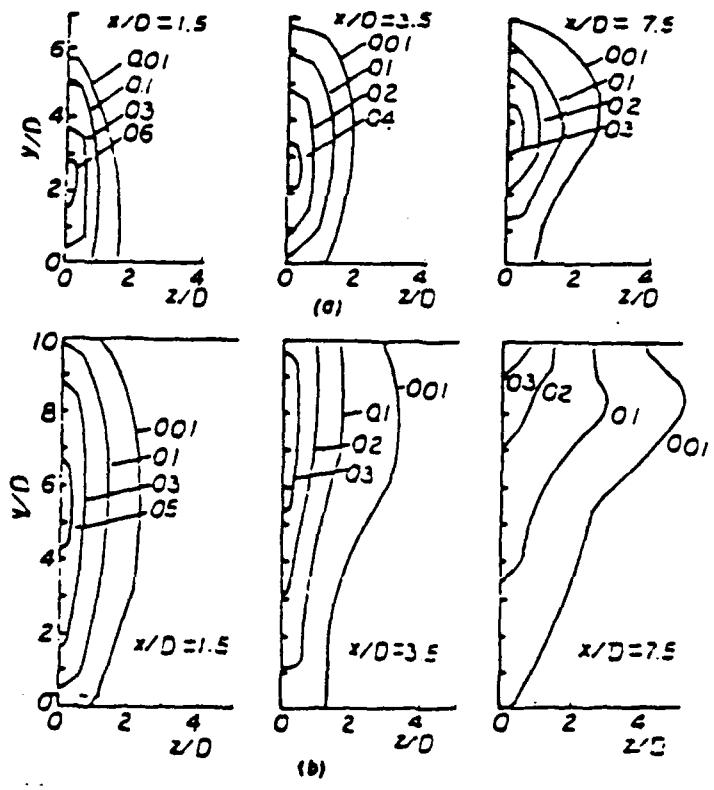Figure 12: Mean Velocity Vectors in x - y plane: (a) R = 2; and (b) R = 4.

Figure 13: Scalar Field C/C_j in y - z Plane at several downstream locations: (a) R = 2; and (b) R = 4.
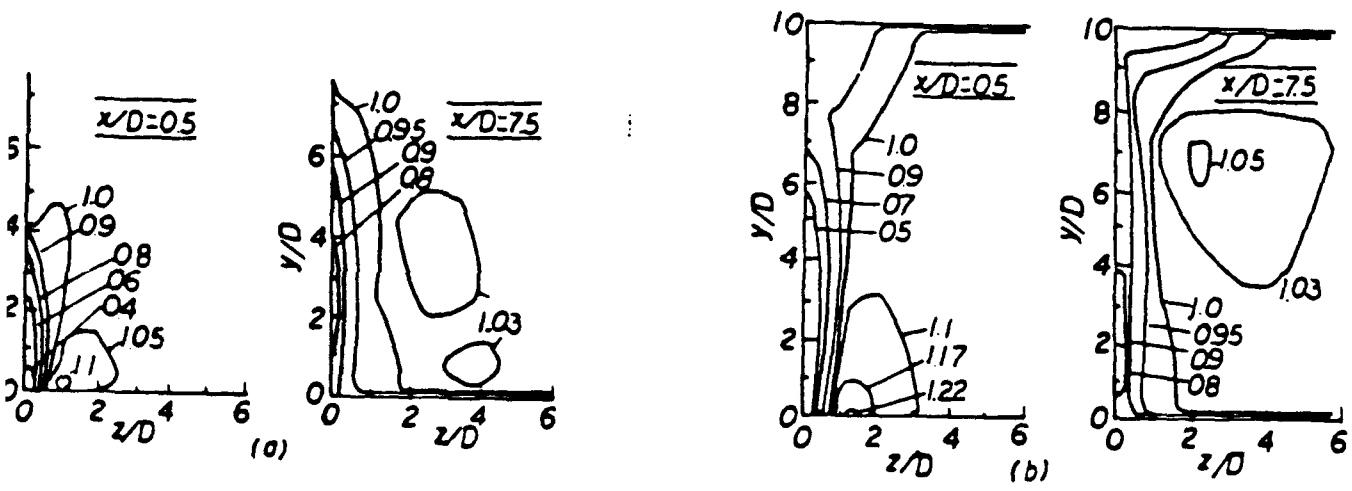

Figure 14: Streamwise Component of Mean Velocity Contours, U/Uo in y-z Plane: (a) R = 2; and (b) R = 4.

directions (y and z directions, respectively). In the case of the higher velocity ratio, the jet stream directly impinges on the opposite plate and diffuses more rapidly in the side direction (z direction). The kidney-shaped cross section of the jet is clearly seen as the jet develops downstream. The point of the maximum scalar value occurs on the top wall and along the centerline after the impingement.

Figure 14 shows contours of the x-direction mean velocity in the y - z planes at two downstream locations. The velocity is nondimensionalized with the cross-stream velocity. In the initial region, the crossflow is accelerated around the edge of the jet and produces a velocity maxima near-side of the jet discharge. In Figure 14, the jet stream gradually gains axial-direction momentum as it is convected downstream. Note that the cross stream is deflected sideways in the initial region. This cross stream then accelerates the jet stream from the edges of the jet cross section after the jet is aligned with the cross stream.

As mentioned previously, a major feature of a jet in a crossflow is the production of the counter-rotating vortices, which are created by the shear along the edge of the jet. Numerical calculations of this study predict the vortex production (Fig. 15). The streamwise component of mean vortices is calculated from the velocity vectors in the cross-section planes. Here, the vorticity is defined as follows:

$$\Omega_x = \frac{\partial(W/U_o)}{\partial(y/D)} - \frac{\partial(V/U_o)}{\partial(z/D)}$$

(67)

Only the vortices in the half-plane extending from the symmetric plane are presented. The opposite half-plane can be visualized with an opposite sign of the vortex strength. The core of the vortex structure in each plane is seen to propagate towards the upper surface as it is convected downstream. The cross-sectional shape of the vortex structure seems to be similar to that of the scalar field drawn in the same

57

cross-section planes except for the wake formed near the bottom wall. It is interesting to note that the vortex structure still exists after the jet impinges on the wall (Figure 15).

Two components of mean velocity are compared with experimental results at four downstream locations in the x-y plane (Figs. 16 and 17). The results show that agreement is generally fair. The main discrepancy, however, is the axial-direction velocity component U, especially in the upstream regions where the flow exhibits strong anisotropy. The streamwise component velocity profiles both at $R = 2$ and $R = 4$ clearly show wake behavior of the flow behind the jet and close to the wall. The wake region is induced by the backflow of the cross stream into the low-pressure region immediately downstream of the jet discharge. The wake region extends downstream but "lifts off" from the lower wall due to the strong inflow of the cross stream towards the symmetric plane. This inward motion carried high-momentum fluid from the cross stream to the symmetric plane. Therefore, the axial component velocity profiles gradually smooth out downstream.

Measurements of the turbulent distributions are presented in Fig. 18 for $R = 4$ at four downstream locations in the x - y plane. The turbulent shear stress $\overline{uv}$ is compared with the calculation of the k - ε model. Again the agreement is less in the initial region. Moving downstream there is a tendency towards an isotropic flow and the agreement improves. The position of the maximum $\overline{u}$ and $\overline{uv}$ profiles corresponds approximately to the center of the jet cross section where the velocity gradients $\partial U/\partial X$ and $\partial U/\partial Y$ are maximum. The $\tilde{v}$ profile maximum corresponds to the edges of the jet where $\partial V/\partial Y$ is maximum. Recalling from the turbulent and mean kinetic energy equation, the maximum transfer energy from the mean flow to the turbulent flow occurs when $\left|\rho\overline{u_i u_j}\right|\left|\partial U_i/\partial X_j\right|$ is maximum. Thus, the turbulent intensities which are an indication of the level of turbulence will be a maximum when the Reynolds stresses and mean velocity gradient are maximum.
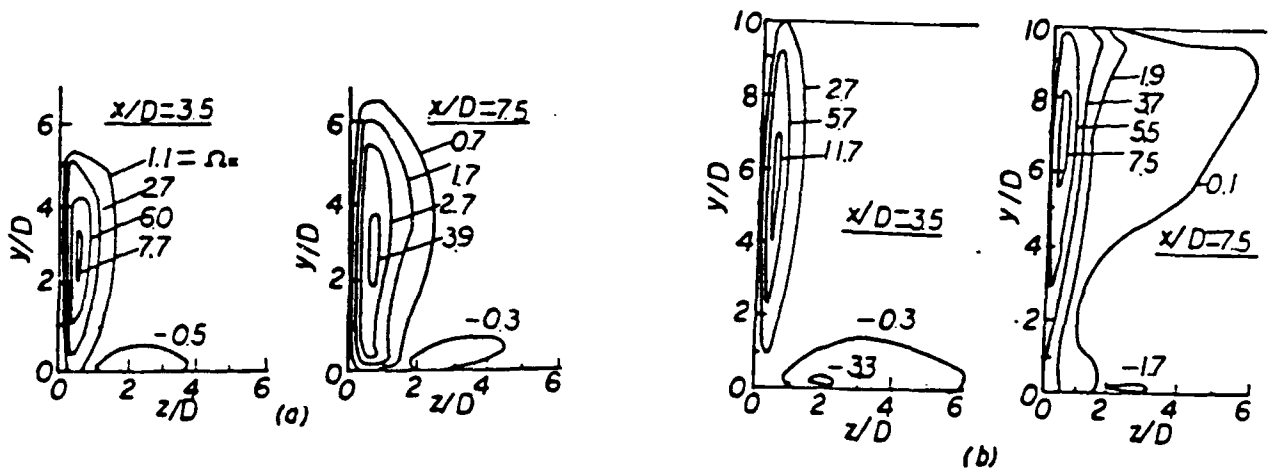
58

Figure 15: Streamwise Component of Mean Vorticity Contours, $\Omega_c = [\partial(W/U_0)/\partial(y/D)] - [\partial(V/U_0)/\partial(z/D)]$: a) R = 2; and b) R = 4.

Figure 16: Comparison between Predicted Profiles and Experimental Data in x - y plane at R = 2. •, measurement and -, prediction: (a) U/U_0; and (b) V/V_J.

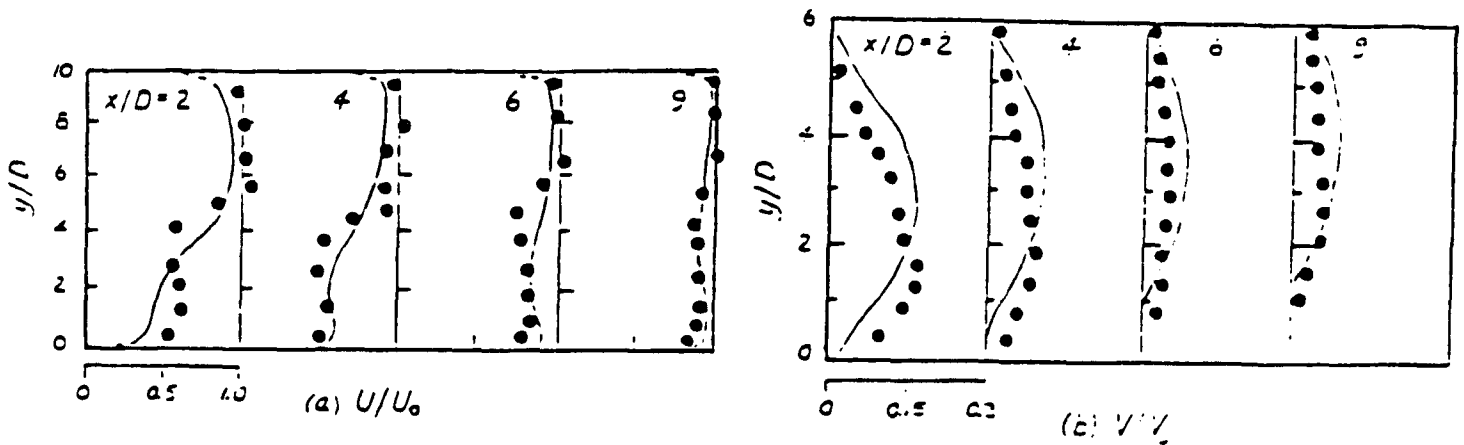Figure 17: Comparison between Predicted Profiles and Experimental data in x-y plane or R = 4; • measurement, -: prediction, (a) U/U_0, (b) V/V_J

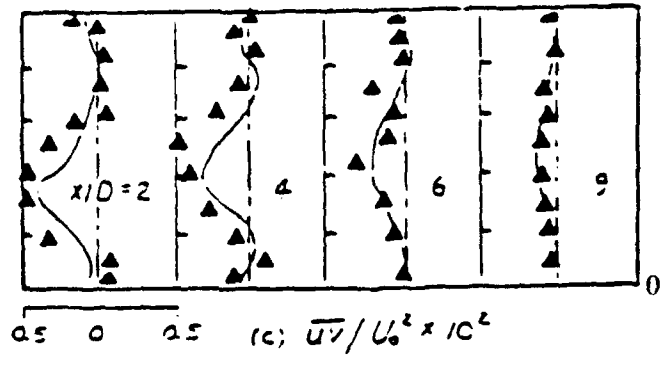(a) U/U_0
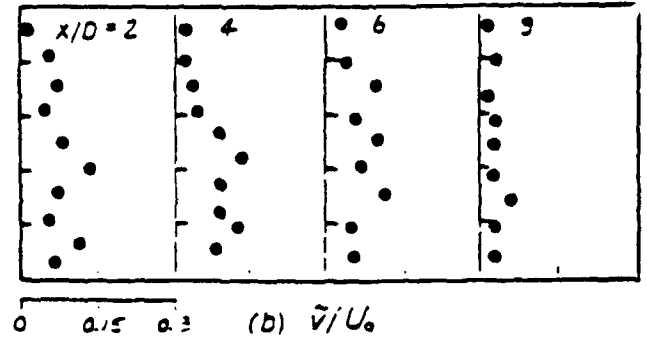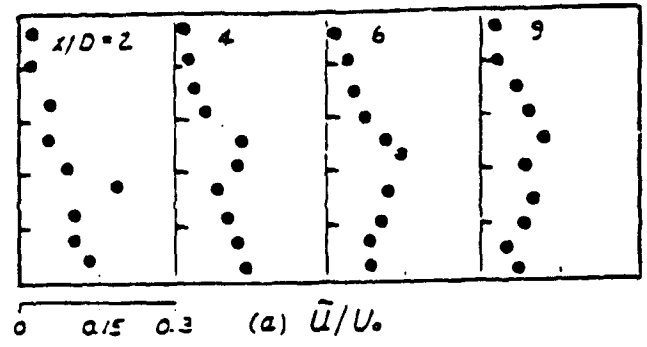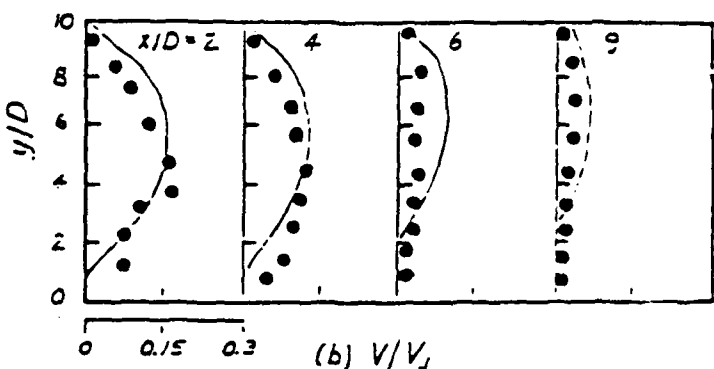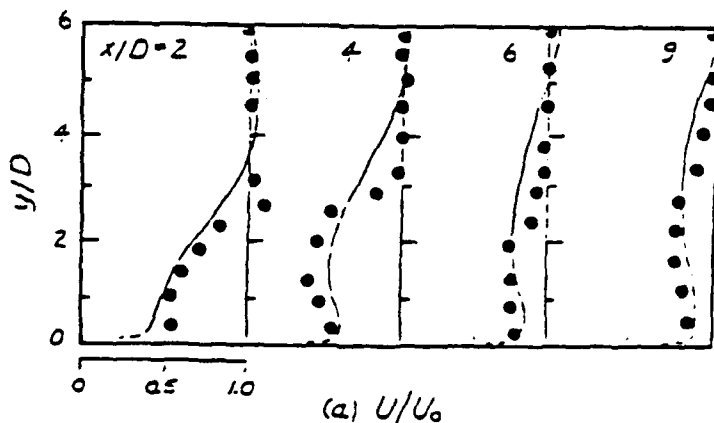
(b) V/V_J

(a) $\tilde{u}/U_0$

(b) $\tilde{v}/U_0$

Figure 18: Normalized Reynolds Stress Distributions in x-y plane at R = 4; (a) $\tilde{u}/U_0$, (b) $\tilde{v}/U_0$, (c) $\widetilde{uv}/U_0^2$

(c) $\overline{uv}/U_0^2 \times 10^2$

Estimates of μ

The dependence of the Reynolds number Re_λ and order n of higher even-order

moments $\overline{\left(\dfrac{\partial u_1}{\partial t}\right)^{2n}} \Big/ \left[\overline{\left(\dfrac{\partial u_1}{\partial t}\right)^2}\right]^n$ for n = 2, 3, 4 is plotted in Figure 19. Frenkiel and

Klebanoff[32], using the properties of the lognormal distribution, showed that:

$$\frac{\overline{\left(\dfrac{\partial u_1}{\partial t}\right)^{2n}}}{\overline{\left(\dfrac{\partial u_1}{\partial t}\right)^2}^{\,n}} \sim \left(\frac{L}{\eta}\right)^{\frac{1}{2}\mu n(n-1)} \sim Re_\lambda^{\frac{3}{4}\mu n(n-1)} \tag{68}$$

under the isotropic assumption that $L/\eta \sim Re_\lambda^{3/2}$. The local slope of the experimental distribution of Figure 19 is proportional to μ and thus the plots shown in Figure 19 can be thought of as a possible method for determining μ. Nine sets of experimental data are presented corresponding to different velocity ratios (λ_j = 1,2,4) and flow locations (x/D = -2,4,8). A straight line has been fitted up to a value of n(n-1) log Re_λ of approximately 20. The arithmetic average value of m is estimated to be 0.38 obtained from a power curve fit with a coefficient of correlation equal to 0.95. It has been suggested by Frenkiel et al.[32] and Antonia et al.[26] that the decrease of μ with n is universal for a given value of f_c in the sense that it does not depend on the particular flow. The present data provide further support for this suggestion. A comparison with the previous results also indicates a slightly higher value of the even order moments.

(a)　Mean Velocity Ratio.　$\lambda_j = 1.0$
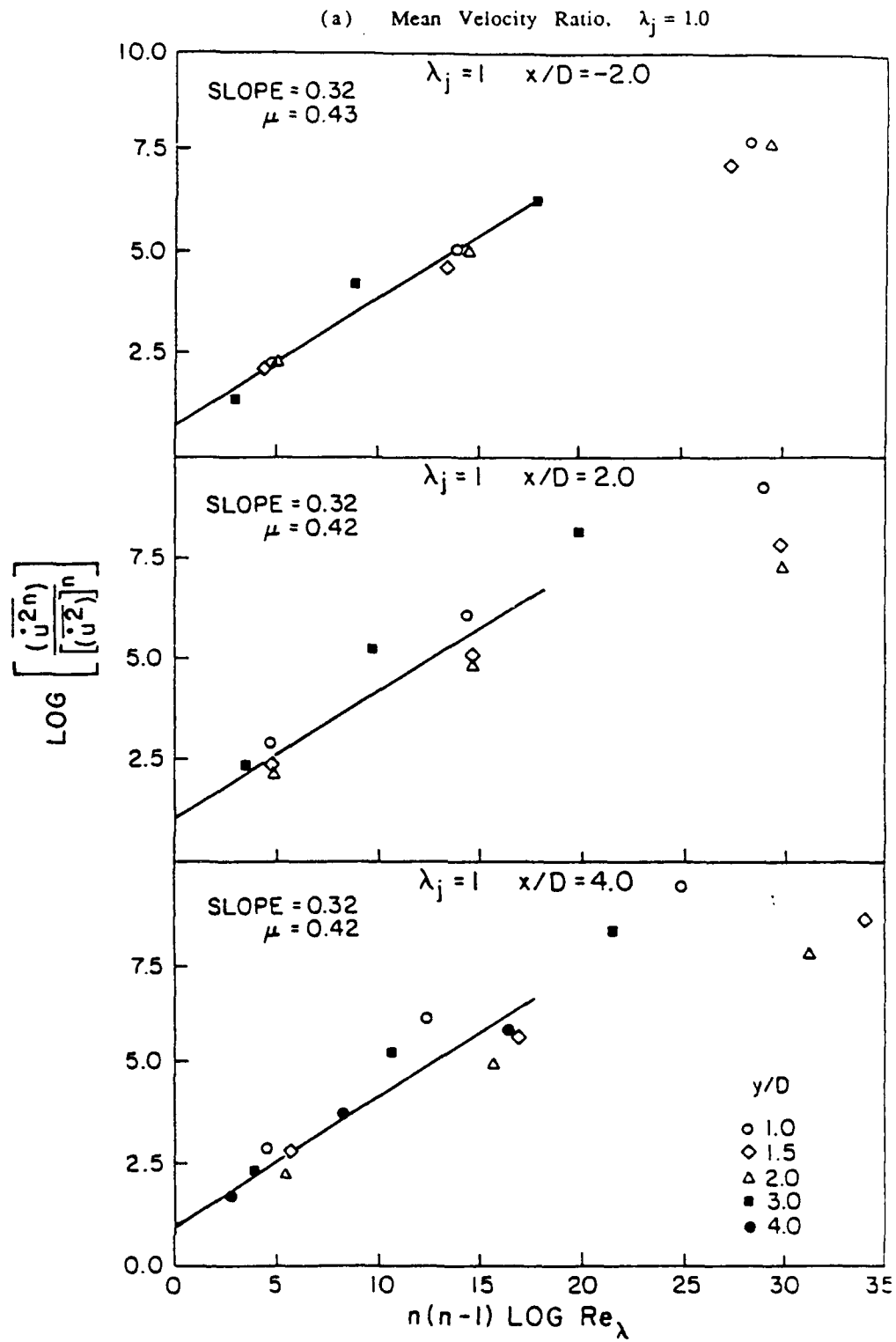
Figure 19 (a): Reynolds Number Dependency of $\dfrac{\left(\overline{\dot{u}^{2n}}\right)}{\left(\overline{\dot{u}^2}\right)^n}$ vs. $n(n-1)\ \log Re_\lambda$; for Various Flow Locations.

62
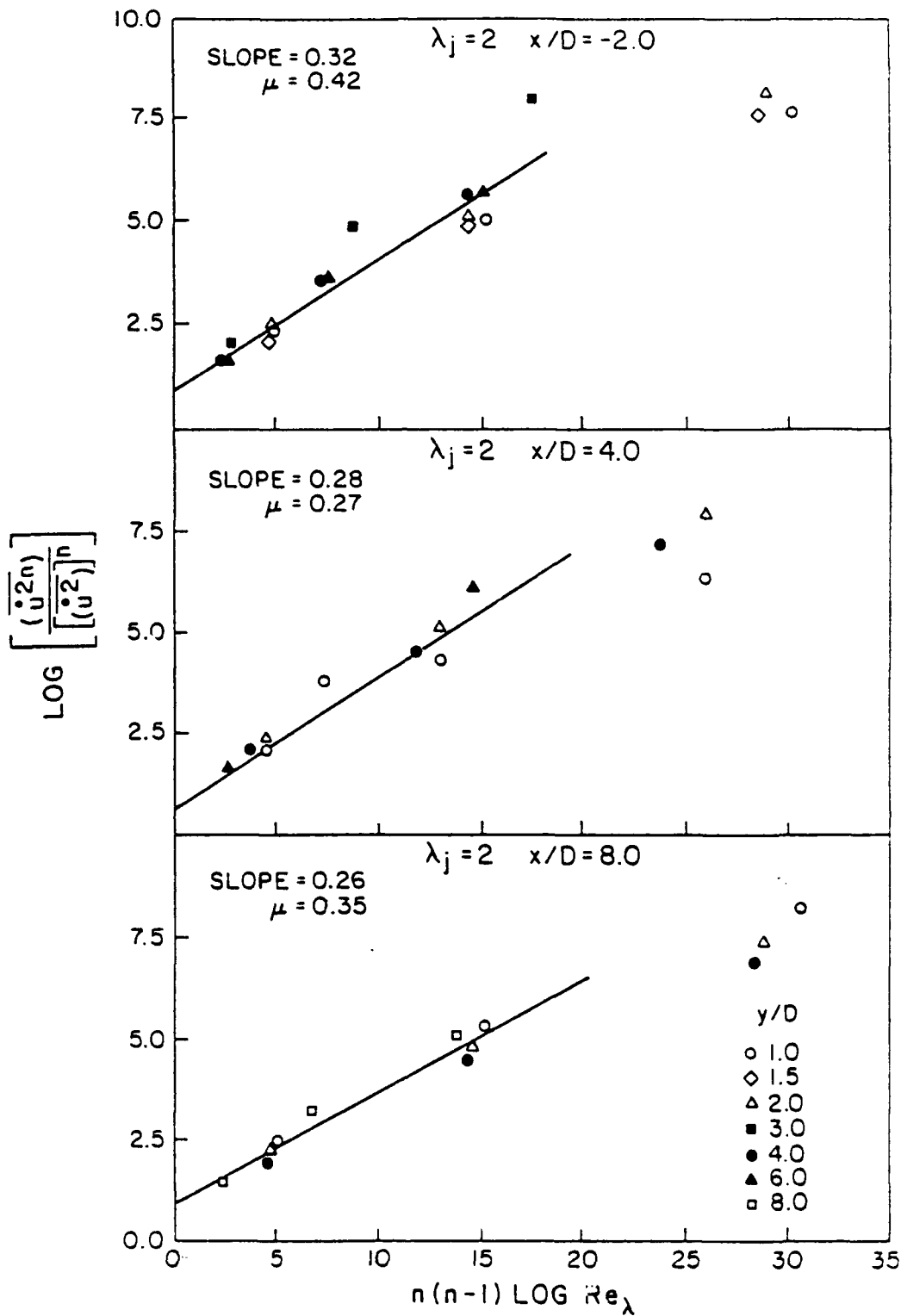
Figure 19 (b): Reynolds Number Dependency of $\dfrac{\left(\dot{u}^{2n}\right)}{\left(\dot{u}^2\right)^n}$ vs. $n(n-1)$ log Re_λ; for Various Flow Locations.

63

(c)   Mean Velocity Ratio, $\lambda_j = 4.0$
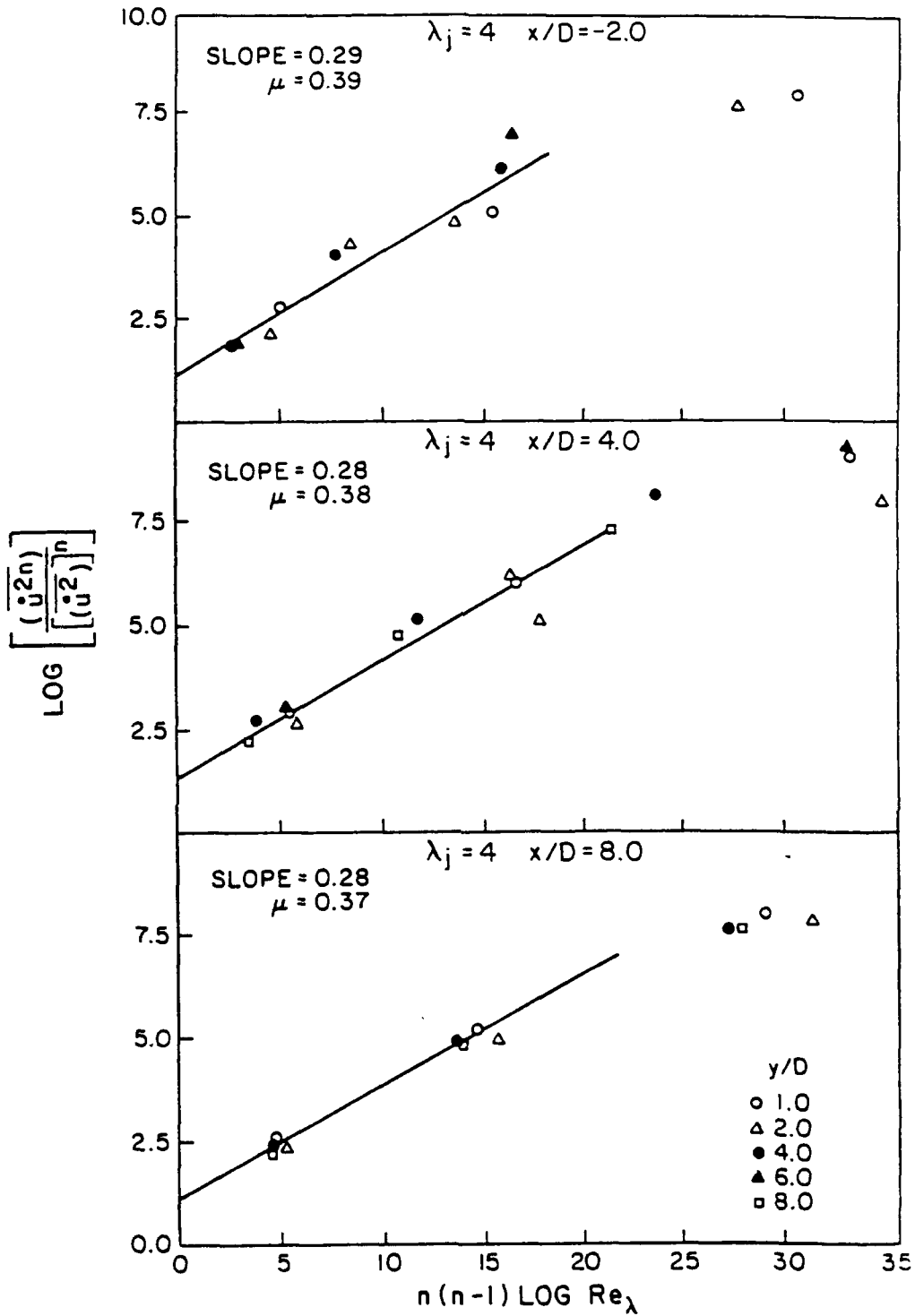
Figure 19 (c):   Reynolds Number Dependency of $\dfrac{\left(\overline{\dot{u}^{2n}}\right)}{\left(\overline{\dot{u}^2}\right)^n}$ vs. n(n-1) log Re_λ; for Various Flow Locations.

64

The implications of these results are significant. First, the magnitude of μ for this particular flow is quite close to the value originally predicted by Yaglom[14] ($\mu = 0.4$). This value is considerably higher than the value proposed by Antonia et al.[26] ($\mu = 0.2$) and less than the estimate of Gibson et al.[25] ($\mu = 0.5$). Secondly, the particular flow field investigated in this work must be considered developing, rather than fully developed. Hence, it would seem arguable that the fully developed restriction may be relaxed and the universal equilibrium theories may apply to the near-field problem in turbulence, as well.

Skewness and Flatness Factors of the Velocity Derivatives

Flatness and skewness factors of $\partial u_1 / \partial t$ are presented in Table 4. Several general observations may be made. First, although the largest flatness values of skewness are found at larger flatness values, distributions with large flatness values appear to be equally likely to have large or small values of skewness. The flatness values range from 30 to 1000. These large flatness values indicate a higher than normal probability of values far from the mean, and the non-Gaussian nature of the derivatives is evident. Predictions of the relationship between flatness and skewness predicted by the lognormal model ($S \propto K^{3/8}$) or by the β-model ($K \propto S^2$) are not indicated by this data. The flatness is seen to increase monotonically with the turbulent Reynolds number.

One-dimensional energy spectra

The one-dimensional energy spectra is $F_1(k_1)$ whose integral over all wavenumbers is $\overline{u_1^2}$. Taylor's approximation in the form $k_1 = 2\pi f / U_1$ was used to transform the frequency f to the wavenumber k_1, the x_1 component. The spectra are presented

Table 4. Statistical Documentation for Various Velocity Ratios and Flow Locations.

Velocity Ratio, $\lambda j = 4.0$

X/D	y/D	ι (m)	λ_T x10^2 (m)	v_k (m/s)	l_k x10^4 (m)	ε (m²/s³)	Re_λ	K	S
+8	+1	.0626	.603	.465	.344	2929	260	335	-5.50
	+2	.0741	.794	.510	.314	4218	407	228	-2.02
	+4	.053	.479	.453	.353	2637	181	245	-0.08
	+6	.0323	.446	.472	.339	3100	178	285	-1.03
	+8	.0544	.550	.353	.454	967	209	134	-2.10
+4	+1	.157	.905	.761	.210	20918	567	624	-2.06
	+2	.128	.711	.740	.216	18727	512	211	1.05
	+4	.0944	.396	.746	.214	19351	114	1367	0.070
	+6	.438	1.25	.495	.323	3750	582	1002	0.065
	+8	.0456	.431	.243	.658	218	63	199	0.085
-2	+1	.0659	.748	.473	.338	3125	358	340	2.10
	+2	.0913	.711	.344	.465	873	197	199	1.06
	+4	.177	.257	.184	.871	713	22.1	66.4	0.95
	+6	.0699	.286	.186	.860	75	24.4	80.1	0.92

Velocity Ratio, $\lambda j = 2.0$

X/D	y/D	ι (m)	λ_T x10^2 (m)	v_k (m/s)	l_k x10^4 (m)	ε (m²/s³)	Re_λ	K	S
+8	+1	.129	.694	.569	.281	6550	384	352	-2.05
	+2	.0421	.543	.553	.289	5860	274	204	2.16
	+4	.0438	.535	.411	.389	1790	243	105	-3.78
	+8	.0146	.199	.166	.965	47.15	15	39.6	-0.088
+4	+1	.0178	.320	.595	.269	7853	158	119	-4.05
	+2	.0283	.366	.587	.272	7440	165	329	-5.47
	+4	.0302	.418	.288	.555	432	99.8	124	-4.56
	+6	.0126	.210	.172	.930	54.7	17.2	52.3	0.075
	+8	.0132	.207	.169	.948	50.77	16.7	33.7	0.011
-2	+1	.130	.735	.518	.309	4503	345	248	0.010
	+2	.0887	.742	.379	.423	1283	262	322	-0.026
	+4	.0188	.239	.158	1.01	39.2	17.2	37.9	-0.028
	+6	.0243	.228	.175	.916	58.3	18.9	41.9	-0.005

Velocity Ratio, $\lambda j = 1.0$

X/D	y/D	ι (m)	λ_T x10^2 (m)	ν_k (m/s)	l_k x10^4 (m)	ε (m^2/s^3)	Re$_\lambda$	K	S
+4	+1	.125	.331	.996	.161	61600	124	824	-4.5
	+1.5	.184	1.04	.667	.240	12300	714	503	2.3
	+2	.0838	.827	.442	.362	2390	425	226	-1.8
	+3	.0241	.376	.246	.651	228	65.2	189	-1.95
	+4	.0214	.278	.170	.943	51.8	24.3	43.6	-0.05
+2	+1	.179	.552	.948	.169	50500	277	756	-2.05
	+1.5	.303	.681	.417	.383	1900	317	269	-1.55
	+2	.0722	.647	.437	.367	2276	326	185	-1.95
	+3	.045	.369	.216	.740	137	48.2	236	-1.95
-2	+1	.0578	.588	.421	.380	1970	214	254	-0.75
	+1.5	.0309	.488	.392	.410	1480	177	157	-1.12
	+2	.0594	.667	.391	.408	1460	258	199	0.08
	+3	.0359	.321	.189	.846	79.9	32.3	74.5	0.65

67

here in Kolmogorov - normalized form, i.e., divided by $(\epsilon v^5)^{1/4}$, in Figure 20(a). The value of the dissipation rate ϵ was estimated from the second moment of the dimensional spectra (Figure 20(b)) using the assumption of dissipative local isotropy, or:

$$\epsilon = 15v \int_0^\infty k_1^2 F_1(k_1)dk. \tag{69}$$

Variation of the functions $(\eta k)^2 \Phi(\eta k)$, $(\eta k)^{5/3} \Phi(\eta k)$ and $(\eta k)^4 \Phi(\eta k)$ with Re_λ is examined. The maximum values from each function are plotted against Re_λ in Figure 21 (a)-(c). Variation of these maximum values was found to vary with the logarithm of Re_λ. For $(\eta k)^2 \Phi(\eta k)$, the relationship:

$$M_1 = 0.0413logRe_\lambda - 0.0326 \qquad 10 < Re_\lambda < 1000 \tag{70}$$

was obtained, where M_1 denotes the maximum value of $(\eta k)^2 \Phi(\eta k)$. The coefficient of correlation for the curve is 0.96. For the function $(\eta k)^{5/3} \Phi(\eta k)$, a similar relationship was found to be (M_2 is the maximum):

$$M_2 = 0.0856logRe_\lambda - 0.171 \quad 10 < Re_\lambda < 1000 \tag{71}$$

with a coefficient of correlation of 0.95. Finally, for $(\eta k)^4 \Phi(\eta k)$, the variation obtained was (M_3 is the maximum):

$$M_3 = 0.1009 - 0.0140logRe_\lambda \qquad 10 < Re_\lambda < 150 \tag{72}$$

with coefficient of correlation 0.98. For values of Re_λ greater than 150, the peak values displayed a decreased dependence on Re_λ.
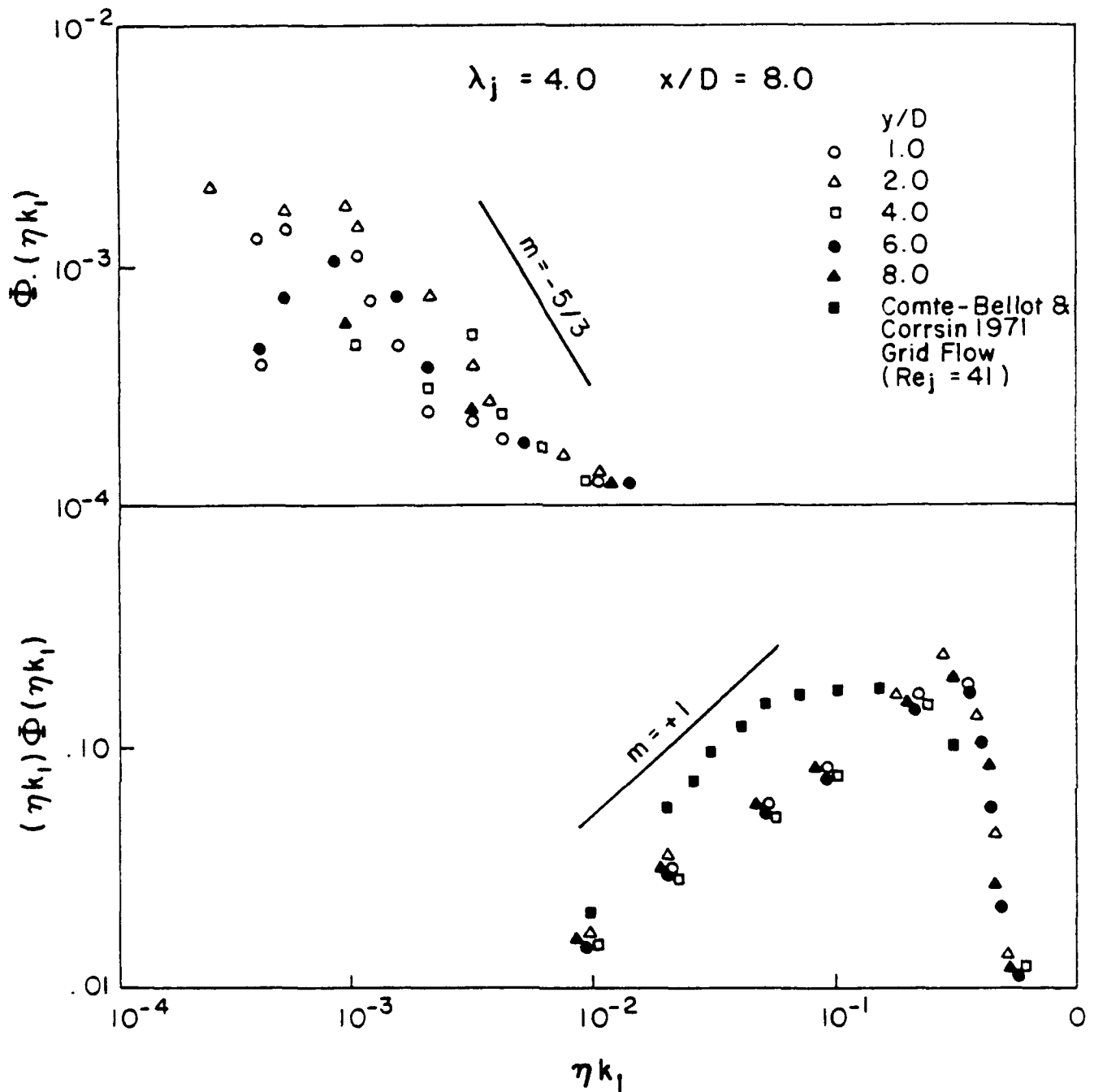
68

Figure 20:   (a)   Example of Typical Nondimensionalized Energy Spectra for
λj = 4.0 and x/D = 8.0 at various locations between the plates.
y/D = 1.0, Re_λ = 260; y/D = 2.0, Re_λ = 407; y/D = 4.0, Re_λ = 189
y/D = 6.0, Re_λ = 178; y/D = 8.0, Re_λ = 209

(b)   Examples of Typical Nondimensionalized Dissipation Spectra for
λj = 4.0 and x/D = 8.0 at various locations between the plates. Com-
parison to Grid Flow Data, from Champagne (33)
y/D = 1.0, Re_λ = 260; y/D = 2.0, Re_λ = 407; y/D = 4.0, Re_λ = 189
y/D = 6.0, Re_λ = 178; y/D = 8.0, Re_λ = 209

Some comparisons with earlier studies can be made. Dissipation spectra from Frenkiel and Klebanoff[32] have been presented. For $Re_\lambda = 60.8$, they found the maximum value of $(\eta k)^2 \Phi(\eta k)$ to be 0.22. For $Re_\lambda = 45.2$, the corresponding maximum was 0.19. The correlation determined in this study, eq. (68), would predict $M = 0.14$ for $Re_\lambda = 60.8$ and $M = 0.12$ for $Re_\lambda = 45.2$. Champagne[33] compiled and graphed $(\eta k)^2$ $\Phi(\eta k)$ from four research sources of varying Reynolds number: (1) a cylinder wake flow, $Re_\lambda = 138$, (2) a grid flow, $Re_\lambda = 41$, (3) a grid flow, $Re_\lambda = 65$, and (4) a homogeneous shear flow, $Re_\lambda = 130$. These curves were found to be very nearly the same, leading Champagne to conclude that the fine-scale structure of the different flow fields is similar at least for the Re_λ range presented here, viz 40-138. The results obtained here indicate that for this developing flow field, Reynolds number independence is not found, neither for $40 < Re_\lambda < 138$, nor for the entire range investigated, $16.6 < Re_\lambda < 782$.

Fractal Dimension of the Dissipation Structure.

The fractal dimension, D, of the dissipation structure was determined from calculations of the turbulent Reynolds number and the flatness of the velocity derivatives at each measuring location. Figure 22 shows a plot of the results. The slope of the line is 0.823, calculated by least-squares nonlinear regression, and having a correlation coefficient of 0.77. The relationship:

$$K \propto Re_\lambda^{3/2(3-D)} \tag{73}$$

becomes:

$$K = 2.72 Re_\lambda^{0.823} \tag{74}$$
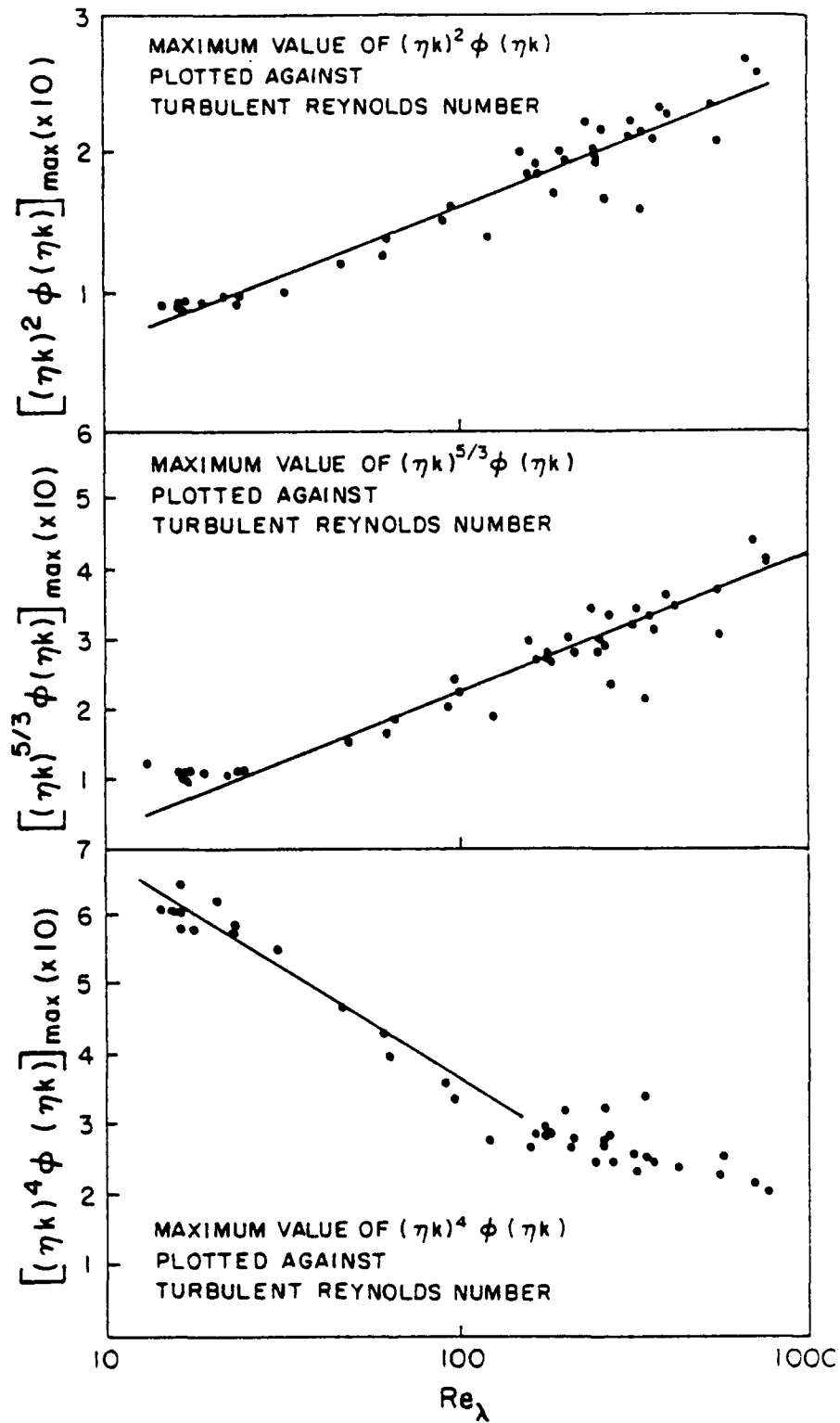
giving a fractal dimension $D = 2.45$.

Figure 21: (a), (b), (c) Maximum Values of $(\eta\, k)^2\, F(\eta\, k)$, $(\eta\, k)^{5/3}\, \Phi\,(\eta\, k)$, and $(\eta\, k)^4\, \Phi\,(\eta\, k)$ plotted versus Turbulent Reynolds Number at Downstream Locations.

71

Sreenivasan and Meneveau[30] reported a fractal dimension value of 2.73 to 2.78, based on a collection of research data. A comparison made of the flatness values in the present work and the other research indicated a possible explanation for the discrepancy. The flatness values found in this study are up to an order of magnitude larger than flatness factors reported elsewhere for flows of comparable Re_λ. Some of the increases may be attributable to the developing nature of the flow in this study, where large variations in velocity occur due to the complex superposition of different flow patterns. However, the developing (versus fully developed) nature of the flow cannot be considered completely responsible for the difference in flatness values. The main reason for the discrepancy, however, may be different measuring techniques used. The velocity derivative values in this research were calculated from digitized velocity data. It is possible that the digital velocity derivative calculations produced high and low values not discriminated by the analog instruments used in earlier studies.

To test what effect such a loss of high and low end data could have on the estimation of D, a "filter" was applied to our data. The width of the filter was set at 12 times the standard deviation of the sample and centered at its mean. New flatness factors were calculated for the filtered data, and found to be substantially lower.

When the filtered data were plotted against Re_λ, as shown in Figure 22, the slope of the resultant line led to a fractal dimension of D = 2.73, exactly in the range estimated by Sreenivasan et al.[30].

Sreenivasan and Meneveau[30] also reported fractal dimensions of the turbulent/nonturbulent surface in several types of turbulent shear flows (boundary layer, axisymmetric jet, plane wake and mixing layer). They found an interface dimension of 2.3 to 2.4 which apparently was independent of the type of flow. It is interesting that the turbulent interface fractal dimension is close to the 2.45 fractal dimension of the dissipation structures.
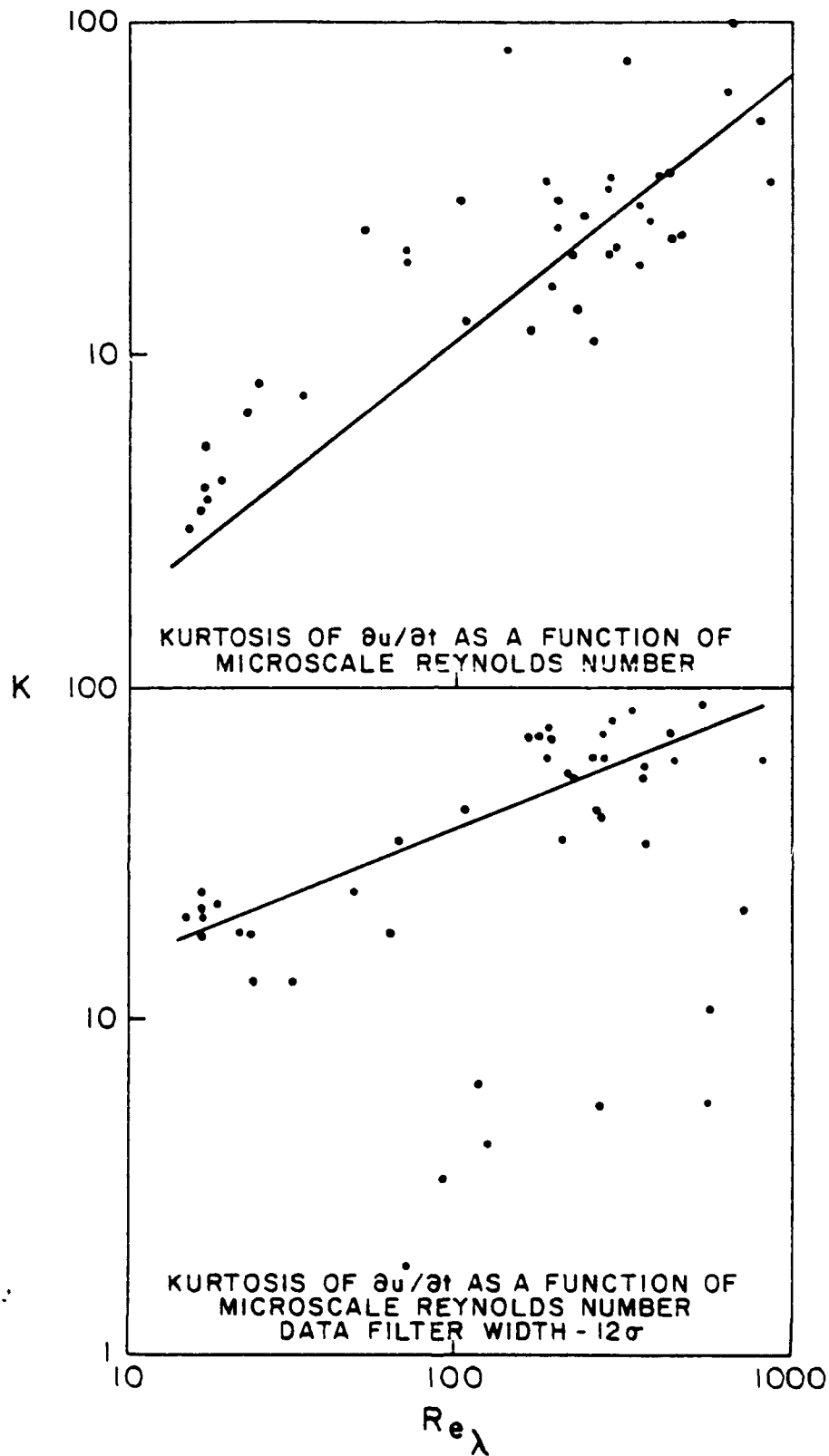
72

Figure 22: (a), (b) Kurtosis of the Velocity Derivative as a Function of the Turbulent Reynolds Number for Two Cases:
(a) Without Numerical Filter
(b) With Numerical Filter, ± 12σ

73

REFERENCES

1. Crabb, D., Durao, D.F.G., and Whitelaw, J.H., "A Round Jet Normal to a Crossflow," Transactions of ASME, _Journal of Fluid Engineering_, Vol. 103, March 1981, pp. 142.

2. Stoy, R.L. and Ben-Haim, Y., "Turbulent Jets in a Confined CrossFlow," Transactions of ASME, _Journal of Fluids Engineering_, Vol. 95, Dec. 1973, pp. 551.

3. Holdeman, J.D. and Walker, R.E., "Mixing of a Row of Jets with a Confined Crossflow," _AIAA Journal_, Vol. 15, Feb. 1977, pp. 243.

4. Kamotani, Y. and Greber, I., "Experiments on Confined Turbulent Jets in a Crossflow," NASA CR-2392, 1974.

5. Durst, F., Melling, A., and Whitelaw, J.H., Principles and Practice of Laser Anemometry, Chapp. 10, 2nd ed., Academic Press, New York, 1981.

6. Launder, B.E. and Spalding, D.B., _Mathematical Models of Turbulence_, Chapp. 5, Academic Press, London and New York, 1972.

7. Patankar, S.V., _Numerical Heat Transfer and Fluid Flow_, Chapp. 6, Hemisphere, Washington, DC, 1980.

8. Demuren, A.O., "False Diffusion in Three-Dimensional Flow Calculations," _Computers and Fluids_, Vol. 13, 1985, pp. 411.

9. Chieng, C.C. and Launder, B.E., "On the Calculation of Turbulent Heat Transport Downstream from an Abrupt Pipe Expansion," _Numerical Heat Transfer_, Vol. 3, 1980, pp. 189.

10. Kolmogorov, A.N., C.R. Acad. Sci. U.R.S.S. Vol. 30, pp. 299, 1941a.

11. Kolmogorov, A.N., C.R. Acad. Sci., U.R.S.S., Vol. 31, pp. 538, 1941b.

12. Kolmogorov, A.N., "A Refinement of Previous Hypothesis Concerning the Local Structure of Turbulence in a Viscous Incompressible Fluid at High Reynolds Number," _Journal of Fluid Mechanics_, Vol. 13, pp. 82-85

13. Obukhov, A.M., "Some Specific Features of Atmospheric Turbulence," _Journal of Fluid Mechanics_, Vol. 13, pp. 77-91, 1962.

14. Yaglom, A.M., Sov. Phys. Dokl., Vol. 11, pp. 26, 1966.

15. Novikov, E.A. and Stewart, R.W., Iz. Akad. Nauk. Scr. Geophys 3, pp. 408, 1964.

16. Frisch, V., Sulem, P.L., and Nelkin, M., "A simple Dynamical Model of Intermittent Fully Developed Turbulence," _Journal of Fluid Mechanics_, Vol. 87, pp. 719-736, 1978.

17. Gurvich, A.S. and Yaglom, A.M., _Physics of Fluids_, Suppl. 10, pp. 559, 1967.

18. Pond, S. and Stewart, R.W., Izv. Atmos. Ocean. Phys., Vol. 1, pp. 530, 1965.

19. Gibson, C.H., Stegen, G.R., and Williams, R.B., "Statistics of Fine Structure of Turbulent Velocity and Temperature Fields at High Reynolds Numbers," Journal of Fluid Mechanics, Vol. 41, pp. 153-167, 1970.

20. Stewart, R.W., Wilson, J.R., and Burling, R.W., "Some Statistical Properties of Small Scale Turbulence in an Atmospheric Boundary Layer," Journal of Fluid Mechanics, Vol. 41, pp. 141-159, 1970.

21. Gibson, C.H., Stegen, G.R., and McConnell, S., "Measurements of the Universal Constant in Kolmogorov's Third Hypothesis for High Reynolds Number Turbulence," Physics of Fluids, Vol. 13, pp. 2448-2451, 1970.

22. Van Atta, C.W. and Chen, W.Y., "Structure Functions of Turbulene in Atmospheric Boundary Layer over the Ocean," Journal of Fluid Mechanics, Vol. 44, pp. 145-159, 1970.

23. Mardelbrot, B.B., "Intermittent Turbulence in Self-Similar Cascades: Divergence of High Moments and Dimensions of Carrier," Journal of Fluid Mechanics, Vol. 62, pp. 331-358, 1974.

24. Van Atta, C.W. and Antonia, R.A., "Reynolds Number Dependence of Skewness and Flatness Factors of Turbulent Velocity Derivatives," Physics of Fluids, Vol. 23, pp. 252-257, 1980.

25. Gibson, C.H. and Masiello, P.J., In Statistical Models and Turbulence (ed. M. Rosenblatt andl C.W. Van Atta), Lecture Notes in Physics, Vol. 12, pp. 427, Springer Verlag, 1972.

26. Antonia, R.A., Phan-Thien, N., and Chambers, A.J., "Taylor's Hypothesis and the Probability Density Functions of Temporial Velocity and Temperature Derivatives in a Turbulent Flow," Journal of Fluid Mechanics, Vol. 100, pp. 193-208, 1980.

27. Bates, C.J. and Hughes, T.D.R., "The Effect of Both Sample Size and Sampling Rate on the Statistical Fluid Flow Parameters in a High Reynolds Number, Low Turbulence Intensity Flow," 5th Bienn. Sympp. on Turbu., Oct. 1977.

28. Cooley, J.W. and Tukey, J.W., "An Algorithm for the Madrine Calculation of Computer Fourier Series," Journal of mathematical Computing, Vol. 19, pp. 297, 1968.

29. Rader, C.M., "An Improved Algorithm for High Speed Autocorrelations with Applications to Spectra Estimation," IEEE Trans. Audio Electronics-Acoustics, 18, pp. 439, 1970.

30. Sreenivasan, K.R. andl Meneveau, C., "The Fractal Facets of Turbulence," Journal of Fluid Mechanics, Vol. 173, pp. 357-386, 1986.

31. Tennekes, H. and Wyngaard, J.C., "The Intermittent Small Scale Structure of Turbulence: Data Processing Hazards," Journal of Fluid Mechanics, Vol. 55, pp. 93-103, 1972.

32. Frenkiel, F.N. and Klebanoff, P.S., "Statistical Properties of Velocity Derivatives in a Turbulent Field," Journal of Fluid Mechanics, Vol. 48, pp. 183-205, 1971.

33. Champagne, F.H., "The Fine Scale Structure of the Turbulent Velocity Field," Journal of Fluid Mechanics, Vol. 86 pt. 1, pp. 67-108, 1978.

34. Antonia, R.A., Satyaprakash, B.R., and Hussain, A.K.M.F., "Fine Scale Velocity Statistics in Turbulent Plane and Circular Jets," Journal of Fluid Mechanics, Vol. 119, pp. 55-89, 1982.

35. Schedvin, J., Stegen, R.G. and Gibson, C.G., "Universal Similarity at High Grid Reynolds Numbers," Journal of Fluid Mechanics, Vol. 65, pp. 561-579, 1974.

36. Tennekes, H. and Lumley, J.L., A First Course in Turbulence, MIT Press, 1972.

37. Sreenivasan, K.R., Chambers, A.J., and Antonia, R.A., Boundary Layer Met., Vol. 14, pp. 341, 1978.

38. ANSI/ASME PTC 19.1, "Measurement Uncertainty," 1984.

39. Andreopoulos, J., "Measurements of a Jet-Pipe Flow Issuing Perpendicularily into a Cold Cross-stream," J. Fluids Engrg., 104, pp. 493, 1982.

40. Andreopoulos, J., "Heat Transfer Measurements in a Heated Jet-Pipe Flow Issuing into a Cold Cross-Stream," Phys. Fluids, 26, pp. 3201, 1883.

41. Catalano, G.D., Chang, K.S., and Mathis, J.A., "Investigation of Turbulent Jet Impingement in a Confined Crossflow," AIAA Journal, Vol. 27, No. 1i, pp. 1530-1535, 1989.

42. Wyngaard, J.C. and Tennekes, H., "Measurements of Small Scale Structure of Turbulence at Moderate Reynolds Numbers," Physics of Fluids, Vol. 13, pp. 1962-1969, 1970.